

**THE MEASUREMENT OF INTERNAL TEMPERATURE
ANOMALIES IN THE BODY USING MICROWAVE
RADIOMETRY AND ANATOMICAL INFORMATION:
INFERENCE METHODS AND ERROR MODELS**

A Thesis Presented

by

TAMARA SOBERS

Submitted to the Graduate School of the
University of Massachusetts Amherst in partial fulfillment
of the requirements for the degree of

MASTER OF SCIENCE IN ELECTRICAL AND COMPUTER ENGINEERING

May 2012

Electrical Engineering

© Copyright by Tamara Sobers 2012

All Rights Reserved

**THE MEASUREMENT OF INTERNAL TEMPERATURE
ANOMALIES IN THE BODY USING MICROWAVE
RADIOMETRY AND ANATOMICAL INFORMATION:
INFERENCE METHODS AND ERROR MODELS**

A Thesis Presented

by

TAMARA SOBERS

Approved as to style and content by:

P. Kelly, Chair

P. Siqueira, Member

C. Salthouse, Member

C. V. Hollot, Department Chair
Electrical Engineering

To my family and victory cot

ACKNOWLEDGMENTS

First I would like to thank my advisor, Professor Patrick Kelly, for his guidance and support while working on this research project. His advice and direction were invaluable and gratefully appreciated. Thank you also to Professor Paul Siqueira and Mr. Benjamin St. Peter for providing their assistance and knowledge pertaining to microwave engineering. I am also grateful to Professor Christopher Salthouse for volunteering and taking the time to be member of my thesis committee.

I would also like to thank the members of the Wireless Systems Lab for their pseudo adoption of me as well as the entire Communications and Signal Processing group.

Finally, I would like to thank my family and friends for their encouraging support and motivation.

ABSTRACT

THE MEASUREMENT OF INTERNAL TEMPERATURE ANOMALIES IN THE BODY USING MICROWAVE RADIOMETRY AND ANATOMICAL INFORMATION: INFERENCE METHODS AND ERROR MODELS

MAY 2012

TAMARA SOBERS

B.Sc., RENSSELAER POLYTECHNIC INSTITUTE

M.S.E.C.E., UNIVERSITY OF MASSACHUSETTS AMHERST

Directed by: Professor P. Kelly

The ability to observe temperature variations inside the human body may help in detecting the presence of medical anomalies. Abnormal changes in physiological parameters (such as metabolic and blood perfusion rates) cause localized tissue temperature change. If the anatomical information of an observed tissue region is known, then a nominal temperature profile can be created using the nominal physiological parameters. Temperature-varying radiation emitted from the human body can be captured using microwave radiometry and compared to the expected radiation from nominal temperature profiles to detect anomalies. Microwave radiometry is a passive system with the ability to capture radiation from tissue up to several centimeters deep into the body. Our proposed method is to use microwave radiometry in conjunction with another imaging modality (such as ultrasound) that can provide the anatomical information needed to generate nominal profiles and improve detection of temperature

anomalies. An inference framework is developed for using the nominal temperature profiles and radiometric weighting functions obtained from electromagnetic simulation software, to detect and estimate the location of temperature anomalies. The effects on inference performance of random and systematic deviations from nominal tissue parameter values in normal tissue are discussed and analyzed.

TABLE OF CONTENTS

	Page
ACKNOWLEDGMENTS	v
ABSTRACT	vi
LIST OF TABLES	x
LIST OF FIGURES	xi
 CHAPTER	
1. INTRODUCTION	1
1.1 Motivation	1
1.2 Why is microwave radiometry interesting for medical applications?	1
1.3 Brief Overview of Radiometry and Principle of Reciprocity	2
1.4 Difficulties using Microwave Radiometry	4
1.5 Contribution	5
1.6 Organization	6
2. GATHERING AND USING ANATOMICAL INFORMATION	8
2.1 Finding Anatomical Information	8
2.2 Modeling Temperature Profiles	9
2.3 Gathering Weighting Functions	14
2.4 Conclusion	18
3. ANOMALY DETECTION AND ESTIMATION METHODS	22
3.1 Detection using GLR <i>without</i> a Signature Dictionary	22
3.1.1 Constructing Temperature Distributions	22
3.1.2 Generating the Hypothesis Tests	24
3.2 Incorporating Signatures in the Detection Algorithm	26

3.2.1	Generating a Signature Dictionary	27
3.2.2	GLR Test Using Signatures	32
3.2.3	Anomaly Location Estimation Using Signatures	36
3.3	Conclusion	36
4.	DETECTION AND ESTIMATION RESULTS	38
4.1	Cube Model Simulation Results	38
4.2	Zubal Model Simulation Results	40
4.3	Discussion of Results	42
4.3.1	Effects of Radiometric Noise	42
4.3.2	The Impact of the Radiometer Location	43
4.3.3	Effects of Anomaly Depth	44
4.3.4	Effects of Anomaly Size	44
4.3.5	Effects of Signature Size	45
4.4	Conclusion	46
5.	EFFECTS OF PARAMETER VARIATIONS	54
5.1	Systematic Error Analysis	54
5.1.1	Dielectric Properties	55
5.1.2	Thermal Conductivities	55
5.1.3	Tissue Layer Thicknesses	55
5.1.4	Metabolic Rate	56
5.1.5	Blood Perfusion Rate	56
5.2	Noise Error Analysis	57
5.3	Conclusion	58
6.	CONCLUSION AND FUTURE WORK	59
	BIBLIOGRAPHY	61

LIST OF TABLES

Table	Page
2.1 Physiological Parameters	12
2.2 Waveguide Dimensions	17
5.1 Variation caused by systematic parameters on the nominal brightness temperature measurements at different frequencies.....	55
5.2 Variation between the abnormal brightness temperature measurements and brightness temperatures with systematic errors in thermal conductivity within the anomalous region.....	56
5.3 Variation between the abnormal brightness temperature measurements and brightness temperatures with systematic errors in metabolic rate within the anomalous region.	57

LIST OF FIGURES

Figure	Page
2.1 2-D Nominal temperature profile of cube model.	12
2.2 1-D Nominal temperature profile of cube model.	13
2.3 2-D Temperature profile with an ischemic anomaly in the cube model.	14
2.4 1-D Temperature profile with an ischemic anomaly centered in the cube model	15
2.5 2-D View of Zupal tissue layout.	16
2.6 2-D View of Zupal nominal temperature profile.	17
2.7 2-D View of Zupal abnormal temperature profile.	18
2.8 1-D Normalized Weighting Function for Cube Model at 2.45 GHz, 3.5 GHz, and 4.5 GHz (linear scale). Note that all of the weighting "bumps" occur within the skull region as seen in Figure 2.10.	19
2.9 1-D Normalized weighting function for the cube model at 2.45 GHz, 3.5 GHz, and 4.5 GHz (log scale).	20
2.10 2-D Cross-section at depth of 1 cm of normalized weighting function for the cube model at 3.5 GHz.	20
2.11 1-D Zupal weighting functions at 2.45 GHz and 3.5 GHz (linear scale).	21
2.12 1-D Zupal weighting functions at 2.45 GHz and 3.5 GHz (log scale).	21
3.1 1-D View of abnormal temperature profiles where the anomaly occurs at two different locations.	30

3.2	Comparison of temperature anomalies generated using the matrix solver and shifting the anomaly.	31
3.3	Comparison of temperature anomalies generated using the matrix solver and shifting the anomaly closer to the skull.	32
4.1	ROC of 16mm deep 10x10x10 anomaly in Cube model with .05°C standard deviation.	40
4.2	Euclidean error estimation results of 16mm deep 10x10x10 anomaly in Cube model with .05°C standard deviation.	41
4.3	ROC of 16 mm deep 10x10x10 anomaly in Cube model with .1°C standard deviation.	42
4.4	Euclidean error estimation results of 16mm deep 10x10x10 anomaly in Cube model with .1°C standard deviation.	43
4.5	ROC of 18mm deep 10x10x10 anomaly in Cube model with .05°C standard deviation.	44
4.6	Euclidean error estimation results of 18mm deep 10x10x10 anomaly in Cube model with .05°C standard deviation.	45
4.7	ROC of 18mm deep 10x10x10 anomaly in Cube model with .1°C standard deviation.	46
4.8	Euclidean error estimation results of 18mm deep 10x10x10 anomaly in Cube model with .1°C standard deviation.	47
4.9	ROC of 19.8mm deep 10x10x10 anomaly in Zubal model with .03°C standard deviation.	47
4.10	Euclidean error estimation results of 19.8mm deep 10x10x10 anomaly in Zubal model with .03°C standard deviation.	48
4.11	ROC of 19.8mm deep 10x10x10 anomaly in Zubal model with .05°C standard deviation.	48
4.12	Euclidean error estimation results of 19.8mm deep 10x10x10 anomaly in Zubal model with .05°C standard deviation.	49
4.13	ROC of 19.8mm deep 12x12x12 anomaly in Zubal model with .05°C standard deviation.	49

4.14	Euclidean error estimation results of 19.8mm deep 12x12x12 anomaly in Zubal model with .05°C standard deviation.	50
4.15	ROC of a <i>centered</i> 18mm deep 10x10x10 anomaly in Cube model with .05°C standard deviation.	50
4.16	ROC of a <i>centered</i> 20mm deep 10x10x10 anomaly in Cube model with .05°C standard deviation.	51
4.17	ROC of a <i>centered</i> 22mm deep 10x10x10 anomaly in Cube model with .05°C standard deviation.	51
4.18	ROC of a <i>centered</i> 16mm deep 6x6x6 anomaly in Cube model with .05°C standard deviation.	52
4.19	ROC of a <i>centered</i> 16mm deep 8x8x8 anomaly in Cube model with .05°C standard deviation.	52
4.20	ROC of a <i>centered</i> 16mm deep 10x10x10 anomaly in Cube model with .05°C standard deviation.	53
4.21	ROCs of a <i>centered</i> 16mm deep 8x8x8 anomaly in Cube model with .05°C standard deviation using different sized signature sets.	53
5.1	The temperature difference between profile with nominal parameters and profile with 10% random variations in nominal parameters.	58

CHAPTER 1

INTRODUCTION

1.1 Motivation

When people are sick, their bodies display symptoms such as an increase in core and localized temperatures in the body. These changes in temperature originate when physiological parameters such as metabolic rate and blood perfusion rate deviate from the norm. For this reason, the ability to detect temperature variations, may aid in detection of diseases/infections as well as characterizing different medical conditions. By using microwave radiometry, the power level of thermal radiation from a tissue region can be captured. If anatomical information of the region is known, then this information can be used with the radiometer power measurements to detect temperature anomalies in the tissue.

1.2 Why is microwave radiometry interesting for medical applications?

As the human body generates heat, thermal radiation is emitted in the microwave spectrum. This thermal radiation can be captured using radiometry, a non-invasive method that measures the amount of energy emitted/released from a source and received at an antenna. Currently, infra-red thermography (the measurement of temperature) has proved useful for detecting temperature anomalies near the skin's surface or anomalies multiple centimeters deep whose temperature increase is large enough such that temperature near the skin increases [13]. Microwave radiometry, however, can respond better to thermal radiation emitted several centimeters below the skin

because of its wavelength spectrum and lower frequency range (between 300 MHz (3×10^8 Hz) and 300 GHz (3×10^{11} Hz))[8]. Microwave radiometry is also a passive process. That is, information can be gathered by solely using a receiving antenna without actively distributing any radiation/signals into the body. Currently, MRI and CT prove useful in medical diagnosis but they may also put patients at risk due to the use of radiation. Recently in the medical imaging community, there has been a push to lower the amounts of radiation used [7], [31], [12].

1.3 Brief Overview of Radiometry and Principle of Reciprocity

Radiometry measures the amount of noise power observed at a receiving antenna. When measuring black bodies, the radiometer receives all of the energy. However, when measuring non-ideal bodies (i.e. the human body), incident energy is partially reflected and not all of the power radiates from the body. As a result, only a fraction of the power radiating is observed at the receiving antenna. This percentage is measured as emissivity (1.1), and the portion of the power observed at the radiometer is the brightness temperature (1.2):

$$e = \frac{P}{kTB} \tag{1.1}$$

$$T_B = eT \tag{1.2}$$

where P is power radiating from the non-ideal body, k is Boltzman's constant, T is temperature of the body, and B is system bandwidth [8]. Emissivity is dependent on the operating frequency as well as the observed volume's properties. Equation 1.2 refers to an object that has uniform temperature and emissivity. For composite objects (like the human body), there is a more complex relationship between the true temperature and the measured brightness temperature. In fact, brightness tempera-

ture can be modeled as the inner product of a weighting function and the temperature profile in an observed object [19]:

$$T_B = \int_{\underline{v}} W(\underline{v}, f) T(\underline{v}) d\underline{v} + T_n \quad (1.3)$$

where \underline{v} is the tissue volume, $T(\underline{v})$ is the temperature distribution in volume \underline{v} , $W(\underline{v}, f)$ is the radiometric weighting function at frequency f over volume \underline{v} , and T_n is the radiometric measurement noise. Previous papers have modeled W as:

$$W(\underline{v}, f) = \frac{P_d(\underline{v})}{\int_{\Omega} P_d(\underline{v}) d\underline{v}} \quad (1.4)$$

where $P_d(\underline{v})$ is the power deposited at \underline{v} by a radiating antenna at the same frequency and of the same form as the radiometer [10]. Weighting functions also have the following properties:

$$\begin{aligned} (i) & W(\underline{v}, f) \geq 0 \text{ for all } \underline{v} \\ (ii) & \int_{\underline{v}} W(\underline{v}, f) d\underline{v} = 1 \end{aligned} \quad (1.5)$$

Weighting functions give more weight to positions in the observed volume that are closer to the antenna's position, versus points that are further away. So while radiometry in principle can be used to measure subcutaneous temperatures, thermal radiation from a location in a volume that is far away from the antenna's position will not contribute much to the brightness temperature.

We assume that the observed volumes are discretized into N voxels. Then the weighting functions, $\{\underline{w}_i, i = 1, \dots, K\}$, calculated at K different frequencies and/or

spatial locations can be treated as a set of linearly independent vectors, and arrayed as columns of a matrix W . Then the vector \underline{T}_B of K brightness temperatures satisfies:

$$\underline{T}_B = W^* \underline{T} + \underline{T}_n \quad (1.6)$$

where \underline{T}_n is the measurement noise K -vector, W is the $N \times K$ matrix of weighting functions, \underline{T} is the discretized true temperature field arranged as an N -vector, and the superscript $*$ denotes adjoint. As noted below, weighting functions for a given tissue configuration can be obtained using electromagnetic simulation software. Other imaging modalities such as MRI or ultrasound can be used to obtain the necessary anatomical information.

1.4 Difficulties using Microwave Radiometry

There are various applications for using radiometric measurements in the clinical setting. Based on the required test, radiometry could be used to generate temperature estimates over an entire volume or a specific region of interest (ROI). Alternatively, these measurements might be used to simply detect the presence of an anomaly in a volume or a restricted ROI. There are some well known difficulties when using microwave radiometry to observe deep tissue temperatures. In particular, in (1.6), there are many more voxels (components of \underline{T}) than there are measurements (components of \underline{T}_B). Therefore, generating temperature estimates is difficult because there are few radiometric measurements available for reconstructing a large temperature field, resulting in an ill-posed problem [35].

The situation can be helped by increasing the number of measurements, varying the receiving antenna's angle, and obtaining the power measurements from different frequencies. Doing so will add more information by increasing the number of weighting functions and improve the chances of projecting the anomaly onto the "weighted"

portion of the weighting functions. However, it is not practically possible to make the problem of reconstructing temperature from radiometry measurements well-posed just by taking more measurements - additional constraints, such as prior distribution on \underline{T} , must be imposed [1].

Some researchers have tried this approach by assuming, for example, that the temperature field must be in the span of a small set of specified basis functions [28], [29]. Another possible approach might be to assume a particular random field model for the temperature, and to find the estimate as a Bayesian reconstruction. In any such approach it would be necessary to ensure that the additional constraints and models are accurate for the temperature field being estimated, so that the estimate is not biased by the assumptions. How best to do this in the case of internal body temperature needs to be the subject of more research. Due to the challenges in estimating \underline{T} , this thesis focuses on the (well-posed) problem of detecting anomalies in \underline{T} based on \underline{T}_B . We also propose a new anomaly location estimation method with the use of a pre-calculated dictionary.

1.5 Contribution

Without knowing the weighting functions and normal temperature distribution, brightness temperatures contain limited information about any anomaly. The general anatomical structure is similar between people but there are slight variations in dimensions such as tissue layer thicknesses. These differences lead to different weighting functions even for identical radiometer configurations, and hence to different brightness temperature vectors between people. Therefore, using an energy detection method that classifies a brightness temperature reading as an anomaly, based on some expected value for the general population might lead to many false alarms because of normal anatomical tissue depth variations.

Again, there are several scenarios for the set of information used to test for anomalies. We might only have the radiometric measurements themselves, along with some basic information such as body core temperature. In some cases (for example, testing for breast cancer [20]) we might be able to take advantage of the body’s contralateral temperature symmetry by using measurements from the opposite side of the body from the location of interest to establish a baseline.

By including anatomical information in the detection process, a baseline can be established to determine what qualifies as nominal versus abnormal radiometric observations for a given individual. The goal of this thesis is to determine how knowledge of anatomical information can impact the detection of subcutaneous temperature anomalies.

We want to consider the case that we have complete knowledge of anatomy in the volume of interest – that is, we know the tissue type at each voxel. Our first objective is to develop hypothesis tests that are in some sense optimal, given radiometric observations and anatomical information, for detecting a deviation from nominal physiological parameter values. We view this work as just a first step in developing a more comprehensive framework for the diagnostic application of microwave radiometry working in conjunction with other modalities.

We first propose a detection process that utilizes the anatomical information to generate nominal brightness temperature. We further exploit the availability of the model to generate multiple anomalous profiles that can be used as a dictionary to improve detection and estimate the location of an anomaly. We also consider how random and systematic errors in each parameter can affect detection rates.

1.6 Organization

This thesis will present a process for detecting temperature anomalies in subcutaneous regions of the body and propose methods for implementation in medical

settings. Chapter 2 explains how anatomical information can be gathered and used to generate weighting functions and temperature profiles. Several imaging modalities that are currently used in clinical settings, could potentially be used for obtaining the information. Using this information, weighting functions can be found using electromagnetic simulation software and temperature profiles can be calculated using Matlab. Chapter 3 covers the derivation of the detection and location estimation algorithms when there is access to anatomical information. Simulation results are presented in Chapter 4 based on the detection and estimation algorithms presented in Chapter 3. In Chapter 5, possible nominal variations are analyzed to determine their impact on the detection algorithm. Chapter 6 summarizes the work presented and proposes directions for future use of radiometry in medical applications.

CHAPTER 2

GATHERING AND USING ANATOMICAL INFORMATION

2.1 Finding Anatomical Information

As noted in the previous chapter, in order to fully use radiometric measurements to capture information about tissue temperatures, we need to couple radiometry to another modality that can provide anatomical information. Methods that might be used to obtain the tissue configuration in a volume include Magnetic Resonance Imaging (MRI), Computed Tomography (CT), and Ultrasound. MRI and CT are expensive procedures whereas Ultrasound is a non-invasive and inexpensive procedure that can be performed at the bedside of a patient. Ultrasound operates by sending high-frequency (2-20 MHz) sound waves into the body and observing how the sound waves are reflected at acoustic impedance boundaries. The differences in acoustic impedance properties make the ultrasound receiver capable of discerning different tissue types and their depths.

Areas of interest for radiometric measurement include the brain, breast, and abdominal regions of the body. Fully modeling an adult head non-invasively would require the use of an MRI or CT scan. However, using one of these devices to detect temperature in the brain (e.g. through the use of MR spectroscopy [6]) may seem inefficient because they are expensive and not as readily available as ultrasound. There is also a concern about radiation dose with CT. In this work, we will focus on the use of a head model obtained from a MRI scan due to the availability of the data. However, the question of how to obtain sufficient anatomical information with minimal cost and risk to the patient is a subject that will need to be explored further.

Ultrasound has several advantages in terms of cost and patient safety. One major limitation with the use of ultrasound for anatomical measurements is that it does not readily pass through bone. However, the use of ultrasound to determine skull and other tissue layer thicknesses has been reported [22],[4]. It should also be noted that in the case of infants and neonates, the skull is not fully formed together and there are soft spots called fontanelles in the head where ultrasound pulses can pass through. This procedure is called a cranial ultrasound and is currently used in clinical settings [14]. Cranial ultrasounds are preferred when observing the brain in neonates due to their minimal discomfort and easy implementation at the bedside.

2.2 Modeling Temperature Profiles

Once a tissue configuration is known, a temperature profile can be generated using the Pennes Bio-Heat Equation (PBE). The PBE is a heat transfer equation that calculates a temperature field in the body based on tissue properties such as metabolic and perfusion rates [16]:

$$\rho_t c_t \frac{\partial T}{\partial t} = \nabla(k \nabla T) + w_b \rho_b c_b (T_{art} - T) + Q_m + Q_r \quad (2.1)$$

where $\rho[kg/m^3]$ is the density, $c[Jkg^{-1}^\circ C^{-1}]$ is the heat capacity, $k[W/^\circ Cm]$ is the thermal conductivity, $w_b[s^{-1}]$ is the blood perfusion rate, $T_{art}[^\circ C]$ is the arterial temperature, $T[^\circ C]$ is the temperature of the local tissue, $Q_m[W/m^3]$ is the metabolic rate, and $Q_r[W/m^3]$ is external heat that is being added or removed from the system. The first assumption is that temperature is steady-state, so $\partial T/dt$ equals zero. We also assume no external heating or cooling (ambient temperature is assumed to be steady-state as well), so Q_r is set equal to zero. This leads to:

$$0 = \nabla(k \nabla T) + w_b \rho_b c_b (T_{art} - T) + Q_m \quad (2.2)$$

Inside a homogeneous region with k assumed to be constant, this can be discretized in a voxelized 3D volume as follows:

$$0 = k \left[\frac{T(x+1, y, z) + T(x-1, y, z)}{\delta_i^2} + \frac{T(x, y+1, z) + T(x, y-1, z)}{\delta_j^2} + \frac{T(x, y-1, z) + T(x, y, z+1)}{\delta_k^2} \right] + w_b(x, y, z) \rho_b c_b (T_{art} - T(x, y, z)) + Q_m(x, y, z) \quad (2.3)$$

where k , w_b , and Q_m are all dependent on the local voxel tissue and δ_i is the voxel size in x , y , or z direction (the equation is slightly modified at tissue region boundaries to account for different values of k). This equation can be rewritten in matrix format as:

$$A\underline{T} = \underline{b} \quad (2.4)$$

where \underline{T} is the temperature vector; A is a sparse matrix whose i^{th} row contains all zeros except at position (i, i) and the six positions corresponding to the nearest neighboring voxels to voxel i :

$$\begin{aligned} A(i, i-s) &= \frac{-k(x, y, z-1)\beta\gamma}{\partial_k^2} \\ A(i, i-l) &= \frac{-k(x-1, y, z)\beta\gamma}{\partial_i^2} \\ A(i, i-1) &= \frac{-k(x, y-1, z)\beta\gamma}{\partial_j^2} \\ A(i, i) &= 1 \\ A(i, i+1) &= \frac{-k(x, y+1, z)\beta\gamma}{\partial_j^2} \\ A(i, i+l) &= \frac{-k(x+1, y, z)\beta\gamma}{\partial_i^2} \\ A(i, i+s) &= \frac{-k(x, y, z+1)\beta\gamma}{\partial_k^2} \end{aligned}$$

where l is the voxel length of the observed volume, s is the number of voxels in a slice of the observed volume, and β and γ are defined as:

$$\beta = \left[\frac{k(x-1, y, z) + k(x+1, y, z)}{\partial_i^2} + \frac{k(x, y-1, z) + k(x, y+1, z)}{\partial_j^2} + \frac{k(x, y, z-1) + k(x, y, z+1)}{\partial_k^2} \right]^{-1}$$

$$\gamma = \frac{1}{1 + \rho_b c_b w(x, y, z) T_{art} \beta}$$

\underline{b} is a vector whose i^{th} entry has the form:

$$b(i) = (\rho_b c_b w T_{art} + Q_m) \beta \gamma \quad (2.5)$$

From (2.4), the PBE becomes a linear algebra problem to solve for \underline{T} . Expanding the PBE into matrix format shows that A is a sparse matrix where there are far fewer non-zero terms compared to the number of zeros in the matrix. Since A is sparse, an iterative sparse matrix solver can be used to solve for \underline{T} . There are various sparse matrix solvers available, but we are limited due to the characteristics of the A matrix. There is no guarantee that A will be symmetric since it is composed of tissue parameters dependent on the volume and it is also extremely large due to the observed volume's dimensions. Based on these characteristics, the Generalized Minimal Residual method solver (GMRES) was chosen.

A temperature field was generated for a cubic model to check if the PBE and iterative solver chosen produced realistic results. Figures 2.1 and 2.2 show the calculated temperature distributions from 2-D and 1-D perspectives. The cube voxels were set to 2mm on each side and consisted of concentric layers of air (2mm), skin (2mm), fat (2mm), skull (6mm), and cerebral spinal fluid (2mm). The interior of the cube was set as brain matter. The cube's size (150 mm x 150 mm x 150mm) was chosen proportional the size of an infant head [18]. The depth of the tissue layers were chosen based on tabulated values for tissue thickness [18] and tissue physiological parameters were obtained from Bardati [10]. The total size of the cube consists then of 75x75x75 (or 421,875) unknowns.

Table 2.1. Physiological Parameters

Tissue Layer	$\kappa(W/^\circ C m)$	$w_b(s^{-1})$	$\rho(kg/m^3)$	$c (Jkg^{-1}^\circ C^{-1})$	$Q_m (W/m^3)$
Air	.026	0	1.3	1006	0
Skin	.343	3.3e-4	1125	3150	360
Fat	.23	3.3e-4	943	2300	302
Skull	.75	0	1850	1300	370
CSF	.60	0	1000	4200	360
Brain Matter	.565	8.4 e-3	1035.5	3680	10000

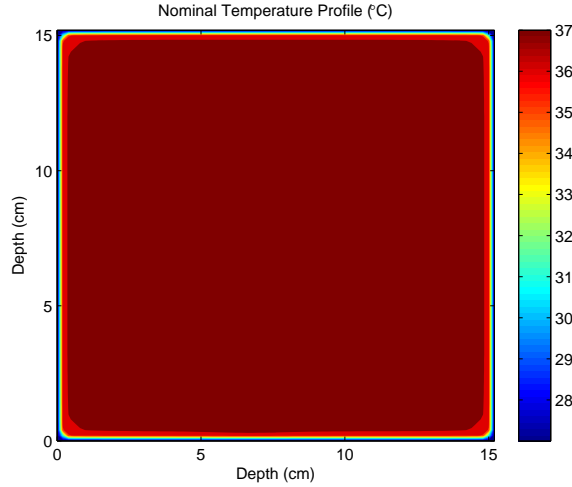


Figure 2.1. 2-D Nominal temperature profile of cube model.

There are various diseases such as cancer, stroke, infections and arthritis that are accompanied by physiological changes that in turn cause tissue temperature to vary from normal values [20],[2],[15],[26]. We wanted to simulate the effect of ischemia (loss of blood flow) in a small region of the brain. Abnormal temperature profiles were generated by setting the blood perfusion rate to zero in a region of 1000 voxels ($8cm^3$). Blood flow acts as a coolant in the PBE so the removal of blood flow should increase the local temperature where the anomaly is taking place. Figures 2.3 and 2.4 show the 2-D and 1-D perspectives of the ischemic temperature profile with the anomaly located in the center of the cube respectively. Temperature increases in the

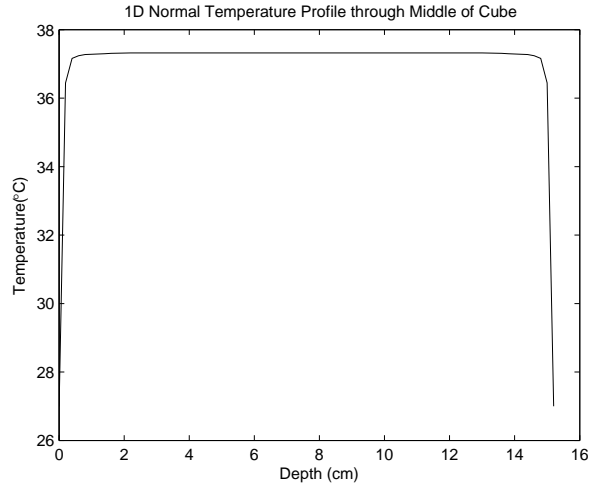


Figure 2.2. 1-D Nominal temperature profile of cube model.

anomaly region which is consistent with experimental findings in cases of ischemic stroke [2].

As noted above, the cube model's dimensions are comparable to an infant child's head and were originally used to determine the detection on a smaller model. An adult head can be modeled using the Zubal head model. The Zubal head model is a set of 128 MRI slices from the head of an adult male that are stacked together. Each slice has 256 voxels in length and width and each voxel is labeled with a tissue type. Each voxel is 1.1 mm in the x and y directions and 1.2 mm in the z direction. Matlab was unable to compute the temperature profile of the original Zubal model due to memory limitations. To reduce the number of voxels, the model was reduced in dimensions to 128 x 128 x 64 voxels by subsampling with each voxels increasing in size to 2.2 x 2.2 x 2.4 mm. The Zubal model is very detailed and consists of tissues such as glands, tendons, etc. Some tissue types in small regions were re-labeled to comparable tissues that were used in the cube model. This needed to be done because of the limited physiological properties available. It should be noted that previous studies have concluded that small tissue structures do not have significant

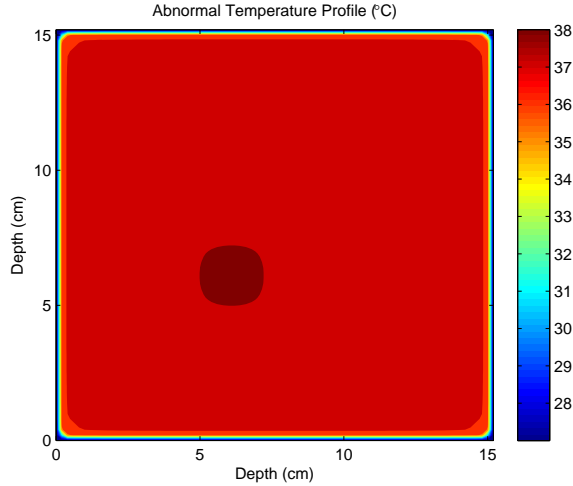


Figure 2.3. 2-D Temperature profile with an ischemic anomaly in the cube model.

effects on temperature or electromagnetic models [5]. There were also some tissues that have the same tissue properties in the model but were labeled based on location within the brain. These tissues were relabeled as well. Figure 2.5 shows the tissue layout in a 2D cross-section of the Zubal model. Temperature fields were found for this model using the same steps as the cube model. Cross-sections of the nominal and anomalous fields are shown in Figures 2.6 and 2.7, respectively, where the anomaly was again an ischemic region of size 10x10x10 voxels.

2.3 Gathering Weighting Functions

The tissue configuration can also be used to obtain the weighting functions. The amount of power measured at the radiometer depends on the antenna’s position in relation to the observed volume and the antenna’s operating frequency. Points in the volume closer to the antenna have a greater impact on the power measured versus points that are further away. These differences in power measurements can be represented in the form of a weighting function that exponentially falls off as the propagation depth into the observed volume increases.

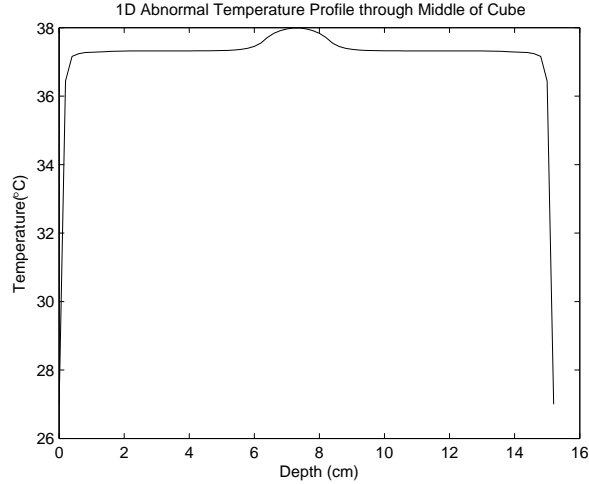


Figure 2.4. 1-D Temperature profile with an ischemic anomaly centered in the cube model

Weighting functions were found by running simulations in Remcom XFDTD [34]. XFDTD is a Finite-Difference Time-Domain Software that is used to solve Maxwell's equations for electromagnetic simulations. For this we used the nominal dielectric properties for tissue presented in [27]; these are summarized in Table 2.1. It is not possible to directly simulate the radiation due to tissue temperature in software. However, the reciprocity theorem in electromagnetics states that the power received at an antenna from a given location is proportional to the power deposited at that location by the antenna operating in the active mode [25]. Therefore, the amount of power that is deposited in a tissue volume can be used to model the amount of power radiated from the same volume, and thus, can be used to find the radiometric weighting function. So instead of treating the body as a source, it is treated as a receiver and the antenna is treated as a source.

Weighting functions were found for the same cube of tissue described in section 2.2 used to create a temperature profile. The antenna used in simulations was a simple monopole antenna mounted inside of a rectangular waveguide that was centered and flush with the face of the cube. The dimensions of the waveguide varied according

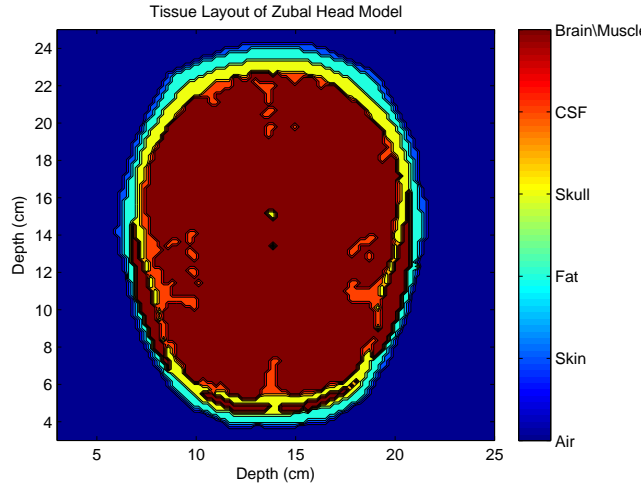


Figure 2.5. 2-D View of Zubal tissue layout.

to the operating frequency [8] (see Table 2.2). A volume sensor was placed around the cube to measure the amount of power deposited by the radiating antenna at 2.45 GHz, 3.5 GHz, and 4.5 GHz. The exported power results were then normalized such that the length of each weighting function summed to unity to create the final set of weighting functions (satisfying 1.5). Figures 2.8 and 2.9 show 1-D perspectives of the normalized weighting functions in linear and log scales respectively. (Note that "bumps" in the weighting function correspond to the location of the skull, which absorbs a relatively high proportion of the input power.) Figure 2.10 shows a 2-D slice of the weighting function at 1 cm deep into the cube in the direction of propagation and demonstrates that the weighting functions fall off exponentially in all directions of propagation.

It is clear from the Figures 2.8 and 2.9 that half way through the cube it is more difficult for the weighting functions to capture any anomalies when the inner product of the weighting function and the temperature profile is computed. This affirms that anomalies that take place at a distance from the radiometer will not have a significant impact on the brightness temperature measured at the radiometer. The

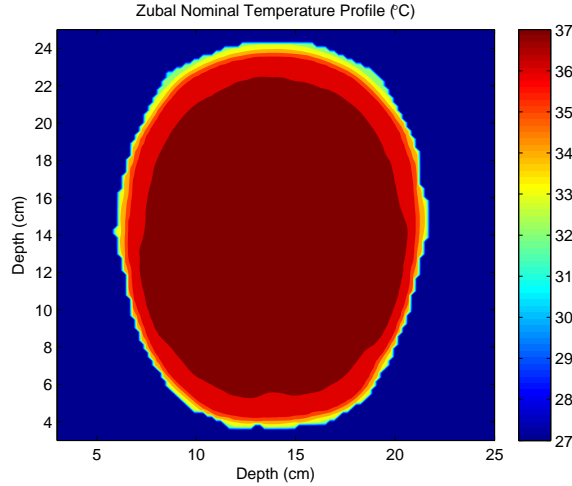


Figure 2.6. 2-D View of Zubal nominal temperature profile.

Table 2.2. Waveguide Dimensions

Frequency (GHz)	Wavelength (m)	Dimensions Inside(cm)	Dimensions Outside(cm)
1.5 (L Band)	.2	16.51 x 8.255	16.916 x 8.661
2.45 (R Band)	.1224	10.922 x 5.461	11.328 x 5.867
3.5 (S Band)	.08577	7.214 x 3.404	7.620 x 3.810
4.5 (HBand)	.066	4.755 x 2.215	5.080 x 2.540

different rates of exponential fall-off also suggest that observing multiple frequency readings at different positions can increase the chances of detecting an anomaly if one is indeed present. Also, since distance between anomaly and radiometer will have a significant impact on detection, the use of multiple sensor locations can be very helpful.

The weighting functions have similar characteristics to the weighting functions used in other papers [10], [11]. Some papers have used equations to calculate weighting functions for simplified tissue configurations, and they have similar characteristics to our simulation results as well.

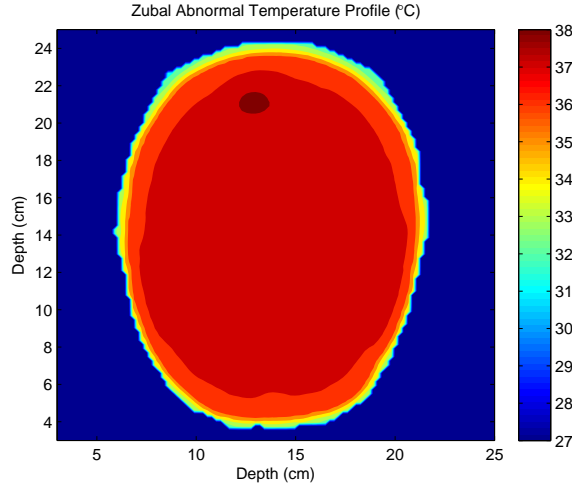


Figure 2.7. 2-D View of Zubal abnormal temperature profile.

Weighting functions were also generated for the Zubal head model using the XFDTD software (Figures 2.11 and 2.12). Since the Zubal model (1,048,576 voxels) is larger than the cube model (421,875 voxels), the time to acquire the weighting functions can take up to 20 minutes. In the future, it may be possible to reduce the time by not regenerating weighting functions for each individual. Instead, the model could be adapted based on the dimensions acquired from the other imaging modalities and used to generate weighting functions.

2.4 Conclusion

This chapter first noted how imaging modalities currently used in clinical settings provide means to obtain the anatomical configuration of an observed region. Anatomical information, along with known values for thermal and physiological parameters of different tissue types, can be used to construct temperature profiles under normal and abnormal conditions. In simulations, ischemia was chosen as the abnormal medical condition. Radiometric weighting functions can also be calculated once anatomical information is known using electromagnetic simulation software. Due to the charac-

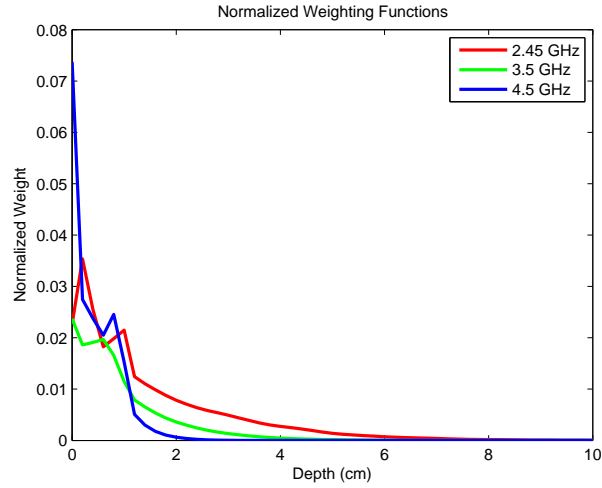


Figure 2.8. 1-D Normalized Weighting Function for Cube Model at 2.45 GHz, 3.5 GHz, and 4.5 GHz (linear scale). Note that all of the weighting "bumps" occur within the skull region as seen in Figure 2.10.

teristics of the weighting functions, different frequencies and antenna locations should provide better insight of possible thermal radiation anomalies at different penetration depths.

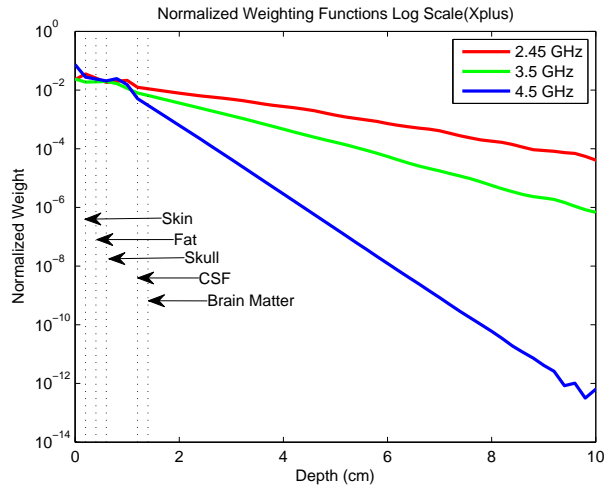


Figure 2.9. 1-D Normalized weighting function for the cube model at 2.45 GHz, 3.5 GHz, and 4.5 GHz (log scale).

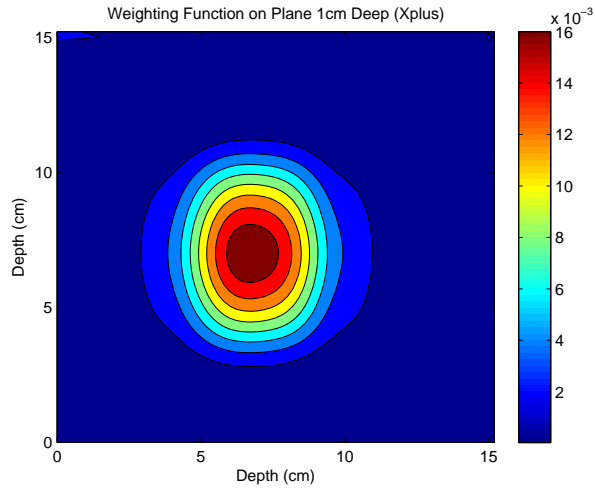


Figure 2.10. 2-D Cross-section at depth of 1 cm of normalized weighting function for the cube model at 3.5 GHz.

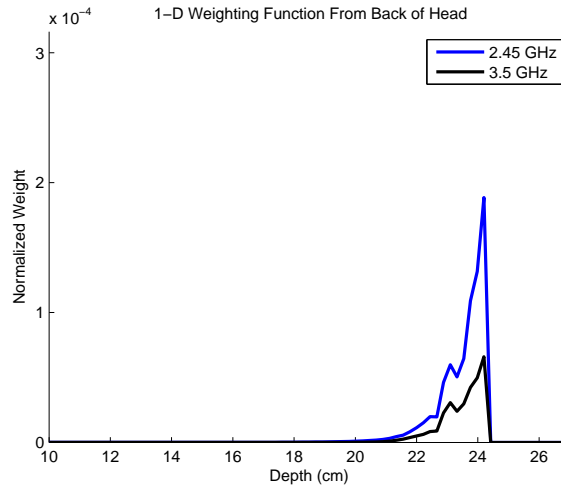


Figure 2.11. 1-D Zubal weighting functions at 2.45 GHz and 3.5 GHz (linear scale).

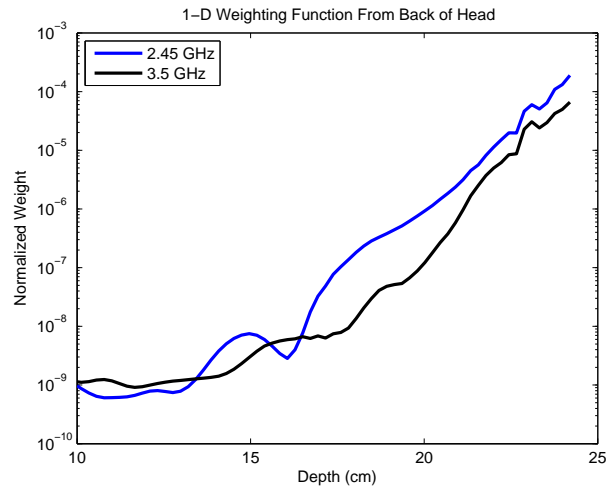


Figure 2.12. 1-D Zubal weighting functions at 2.45 GHz and 3.5 GHz (log scale).

CHAPTER 3

ANOMALY DETECTION AND ESTIMATION METHODS

In this chapter, we will derive detection algorithms that determine if a temperature anomaly is present in an observed volume. The important contribution is that anatomical information is included in the detection process. Without anatomical information, power measurements could not be compared against nominal brightness temperature based on an individual's nominal temperature profile. The first detection algorithm presented incorporates the nominal brightness temperature in the detection process. Two more algorithms are derived that use a set of pre-calculated signatures for abnormal brightness temperatures to improve performance rates.

Each detection algorithm presented uses a hypothesis testing framework to compare normal temperature patterns/profiles versus abnormal temperature patterns using the probability distributions of the nominal and abnormal power measurements. The unknown size and location of an anomaly are accounted for through use of a Generalized Likelihood Ratio test (GLR). The following steps will show how the GLR test is constructed. Results of the detection algorithms are presented in Chapter 4.

3.1 Detection using GLR *without* a Signature Dictionary

3.1.1 Constructing Temperature Distributions

We want to construct hypothesis tests where the observation \underline{T}_B is used to determine if an anomaly is present. Hypothesis H_0 will represent the condition that the observation is under nominal conditions and H_1 will represent the condition that

an anomaly is present. Under H_0 , physiological parameters take their nominal values, which leads to nominal (expected) brightness temperature vector $\underline{T}_{B,0} = W^* \underline{T}_0$, where $A_0 \underline{T}_0 = \underline{b}_0$ and \underline{T}_0, A_0 , and \underline{b}_0 are respectively the nominal body temperature field, the bioheat matrix, and the bioheat vector. In practice, there may be variations from nominal parameter values even under what might be considered normal conditions. The effect of these will be to generate variations from the expected nominal brightness temperature vector $\underline{T}_{B,0}$. We model these variations as being Gaussian and mean zero, with a covariance matrix C . (The effects of nominal parameter variations will be considered in more detail in Chapter 4.) We also assume that the radiometer noise is an independently and identically distributed (IID) Gaussian random vector \underline{T}_n with each component having variance σ^2 . Then under H_0 the observed brightness temperature under nominal conditions has the distribution:

$$\underline{T}_B \sim N(\underline{T}_{B,0}, R) \quad (3.1)$$

where N denotes a normal (Gaussian) distribution and $R = C + \sigma^2 I$.

Under the hypothesis H_1 , abnormal physiological parameter values deviate from the norm and introducing anomalies A_a and \underline{b}_a into the values of the bioheat matrix and vector, respectively. As a result, anomaly \underline{T}_a occurs in the body temperature field and $\underline{T}_{B,a} = W^* \underline{T}_a$ in the brightness temperature vector. The PBE is then:

$$(A_0 + A_a)(\underline{T}_0 + \underline{T}_a) = \underline{b}_0 + \underline{b}_a \quad (3.2)$$

which reduces to $(A_0 + A_a)\underline{T}_a = \underline{b}_a - A_a \underline{T}_0$; and

$$\underline{T}_B \sim N(\underline{T}_{B,0} + \underline{T}_{B,a}, R) \quad (3.3)$$

Note that we assume that the covariance matrix is the same for nominal and abnormal temperature distributions. The main difference between the distributions is that the mean of the abnormal distribution is shifted away from that of the nominal distribution.

3.1.2 Generating the Hypothesis Tests

If f_0 and f_1 denote the probability density functions under H_0 and H_1 respectively, then with these models the likelihood ratio for testing for an anomalous temperature is:

$$\begin{aligned} \frac{f_1(\underline{T}_B | \underline{T}_{B,0}, \underline{T}_{B,a})}{f_0(\underline{T}_B | \underline{T}_{B,0})} &= e^{-\frac{1}{2} \{ \langle \underline{T}_B - \underline{T}_{B,0} - \underline{T}_{B,a}, R^{-1}(\underline{T}_B - \underline{T}_{B,0} - \underline{T}_{B,a}) \rangle - \langle \underline{T}_B - \underline{T}_{B,0}, R^{-1}(\underline{T}_B - \underline{T}_{B,0}) \rangle \}} \\ &= e^{\frac{1}{2} \{ 2 \langle \underline{T}_B, R^{-1} \underline{T}_{B,a} \rangle - \langle \underline{T}_{B,a}, R^{-1}(2\underline{T}_{B,0} + \underline{T}_{B,a}) \rangle \}} \end{aligned} \quad (3.4)$$

First, suppose that we do not have anatomical information, so we do not know $\underline{T}_{B,0}$ or the exact value of R . With no specific knowledge of the brightness temperature due to normal physiological variations, it is reasonable to model R as some constant σ^2 times the identity matrix I . In that case, the likelihood ratio (3.4) reduces to:

$$e^{\frac{1}{2\sigma^2} \{ 2 \langle \underline{T}_B, \underline{T}_{B,a} \rangle - \langle \underline{T}_{B,a}, (2\underline{T}_{B,0} + \underline{T}_{B,a}) \rangle \}} \quad (3.5)$$

Note that for any fixed value of $\underline{T}_{B,0}$ and $\underline{T}_{B,a}$ the likelihood ratio monotonically increases with $\langle \underline{T}_B, \underline{T}_{B,a} \rangle$. Assuming that we are trying to detect a medical condition which would produce an increase in temperature, where $\underline{T}_{B,a}(k) > 0$ for $k = 1, \dots, K$ with K radiometric measurements, then any increase in $\|\underline{T}_B\|$ will lead to a larger value for the likelihood ratio. So, in absence of any specific knowledge of the values of $\underline{T}_{B,0}$ and $\underline{T}_{B,a}$, it is reasonable to use an energy-based test for an

anomalous temperature increase by using a test statistic that increases with the size of $||\underline{T}_B||$ - for example:

$$h = ||\underline{T}_B||^2. \quad (3.6)$$

Now suppose that we have access to anatomical information that can be used to find A_0 , \underline{b}_0 , and W . Then the normal brightness temperature $\underline{T}_{B,0}$ can be calculated using (1.3). By defining the centered observation as $\underline{U} = \underline{T}_B - \underline{T}_{B,0}$, the log likelihood ratio (that is the log of 3.4) can be written as:

$$\langle \underline{U}, R^{-1}\underline{T}_{B,a} \rangle - \frac{1}{2} \langle \underline{T}_{B,a}, R^{-1}\underline{T}_{B,a} \rangle \quad (3.7)$$

Since the exact form of $\underline{T}_{B,a}$ is unknown, the likelihood ratio cannot be computed directly. Instead we use a Generalized Likelihood Ratio test. That is, we form a test statistic by substituting the maximum likelihood estimate of $\underline{T}_{B,a}$ under H_1 in the log-likelihood ratio. If we assume the abnormal temperatures are positive, but impose no other restrictions, then because of the nature of the weighting functions, it follows that the anomalous brightness vector can only hold positive values. Therefore, the ML estimate of the anomalous brightness temperature, $\hat{\underline{T}}_{B,a}$, is the solution to the constrained optimization problem:

$$\text{Minimize } \langle \underline{U} - \underline{T}_{B,a}, R^{-1}(\underline{U} - \underline{T}_{B,a}) \rangle \text{ such that } \underline{T}_{B,a}(k) \geq 0 \text{ for } k = 1, \dots, K \quad (3.8)$$

From the Kuhn-Tucker conditions on the solutions to optimization problems with inequality constraints [33], the solution to this problem has the form:

$$\hat{\underline{T}}_{B,a} = \underline{U} + R\underline{d} \quad (3.9)$$

where \underline{d} is a vector such that $d(k) \geq 0$ for each k ; $d(k) = 0$ when $\hat{\underline{T}}_{B,a}(k) > 0$; and $\hat{\underline{T}}_{B,a}(k) \geq 0$ for each k . When this is solved for $\hat{\underline{T}}_{B,a}$ and \underline{d} , and $\hat{\underline{T}}_{B,a}$ is substituted

for $\underline{T}_{B,a}$ in (3.7), we get the GLR test statistic $\langle \underline{U}, R^{-1}\underline{U} \rangle - \langle \underline{d}, R\underline{d} \rangle$. If we assume that $R = \sigma^2 I$, then we have the maximum likelihood estimate:

$$\hat{T}_{B,a}(k) = \begin{cases} U_k, & U_k \geq 0 \\ 0, & otherwise \end{cases}$$

and the GLR test statistic reduces to:

$$\gamma = \|\underline{U}\|^2 + \|\underline{d}\|^2 \tag{3.10}$$

$$= \sum_{k=1}^K V_k^2 \tag{3.11}$$

where

$$V_k = \begin{cases} U_k, & U_k \geq 0 \\ 0, & else \end{cases}$$

Note that this discounts cases when the observed brightness temperature is smaller than the nominal expected value since we are assuming an anomaly that causes an increase in temperature. A threshold on γ will be used to classify a power measurement reading as nominal, H_0 , or abnormal, H_1 . As will be shown in the test results in Chapter 4, comparison of this statistic (3.11) with statistic h defined previously in (3.6) shows having anatomical information improves the detection of anomalies.

3.2 Incorporating Signatures in the Detection Algorithm

This section presents a GLR test that can further exploit the availability of anatomical information to improve detection. Since we have the ability to generate brightness temperature profiles for given tissue configurations and values for physiological parameters, we can also generate abnormal brightness temperature measurements due to anomalies at different locations in the model. If we run the anomalous

temperature fields through the weighting functions matrix, we will generate the expected brightness temperature signatures of anomalies in different tissue locations. By providing more information about the expected observation due to a temperature anomaly, we would expect that the signatures could be used to improve anomaly detection. These measurements will also provide insight about the anomaly location by determining at what location an anomaly generates brightness temperatures very close to the observed anomalous brightness temperature. In the following we first describe how the properties of the terms in the bio-heat equation enable us to compute sets of anomaly signatures with reasonable effort. Then we develop detection and location estimation algorithms that make use of the signature dictionary.

3.2.1 Generating a Signature Dictionary

Suppose that we are looking for a tissue anomaly of a specified type, characterized by some anomalous physiological parameters (metabolic and perfusion rates). Suppose also that we can specify a shape for the anomalous region (e.g. a sphere of a certain size). We want to characterize expected anomalous brightness temperature vectors (that is, the observed signatures) that result from the anomalous region being placed in different tissue locations. If we follow the same steps used to generate the temperature profiles in section 3.2, sparse matrix solvers would be used to calculate the temperature profile as an anomaly is moved throughout the model. This task becomes a long computational problem that is also dependent on the number of profiles generated. However, we propose to exploit similarities of temperature anomalies within the same tissue region to regenerate anomalous temperature profiles without multiple uses of the sparse matrix solver.

Note first that, from equation 2.4, the matrix A in the discretized form of the Pennes bio-heat equation is very sparse, with the row corresponding to tissue voxel \underline{u} having non-zeros entries only at the diagonal $(\underline{u}, \underline{u})$ and the six components cor-

responding to the nearest-neighboring voxels of \underline{u} . So, a physiological anomaly at a voxel affects at most seven rows of A , out of many thousands of rows in the full matrix, and for a voxel in the interior of a tissue region the configuration of the changed entries is constant except for a position shift as the voxel is moved. That is, the system of equation 3.12 that defines the anomalous temperature field is nearly shift-invariant with respect to shifts that keep a small physiological anomaly in the interior of a given tissue region. Since the nominal temperature profile is known, ($A_0\underline{T}_0 = \underline{b}_0$), we can subtract these terms from both sides of the equation.

$$\begin{aligned}
A_0\underline{T}_0 + A_0\underline{T}_a + A_a\underline{T}_0 + A_a\underline{T}_a &= \underline{b}_0 + \underline{b}_a \\
A_0\underline{T}_a + A_a\underline{T}_0 + A_a\underline{T}_a &= \underline{b}_a \\
(A_0 + A_a)\underline{T}_a &= \underline{b}_a - A_a\underline{T}_0 \\
\underline{T}_a &= (A_0 + A_a)^{-1}(\underline{b}_a - A_a\underline{T}_0) \quad (3.12)
\end{aligned}$$

Because of the shift-invariance property of the anomalous temperature, instead of adjusting physiological properties and using the sparse matrix solver, numerous signatures can be created by shifting the temperature contribution of the anomaly throughout the temperature profile. That is if the anomalous temperature field due to a small region with abnormal physiology centered at voxel \underline{v}_0 is $T_{a,\underline{v}_0} = \{T_{a,\underline{v}_0}(\underline{v}), \underline{v} \in V\}$, then the field due to the same abnormality shifted to be centered at voxel \underline{v}_1 is $T_{a,\underline{v}_1} \approx \{T_{a,\underline{v}_0}(\underline{v} - [\underline{v}_1 - \underline{v}_0]), \underline{v} \in V\}$.

This practical method reduces the computational time it takes to generate over hundreds of signatures from hours to minutes. The brightness temperature vector for each anomalous temperature profile can then be calculated by applying the weighting function matrix W^* by calculating $\underline{T}_{b,a} = W^*\underline{T}_a$. Each set of brightness temperatures are normalized so that the norm of each signature set equals one. The result is a

dictionary of anomalous brightness temperature vectors, say $\{\underline{s}_{a,m} = W^* \underline{T}_{a,v_m}\}$ for anomalies centered at some selected set of voxels $\{\underline{v}_m, m = 1, \dots, M\}$.

As an example, we observed two 1000 voxel anomalies placed within the cube model. One anomaly occurs in the center of the cube and another is off-centered. The temperature fields were calculated using the sparse matrix solver. Once the nominal temperature profile is subtracted, the increase in temperature and fall off appear to be identical (Figure 3.1). Next, the anomalous temperature fields were calculated by subtracting the nominal temperature field. As shown in Figure 3.2, except for a position shift the two anomalous patterns are nearly identical.

It should be noted that anomalies that occur near the skull are expected to produce different anomalous temperature increases compared to anomalies that do not occur near tissue discontinuities. For example, in the cubic head model, there is a bigger difference when the anomaly occurs closer to the skull (Figure 3.3).

We now consider how the brightness temperature vector for a given anomaly may be represented by the signatures in the dictionary. Now we can note some properties of the anomalous matrix A_a . The physiological changes that characterize anomalies of interest to use are variations from the nominal metabolic and blood perfusion rates. Metabolic rate does not contribute to A , so it does not factor in A_a . A change in blood perfusion rate at a given voxel affects only the diagonal entry of A corresponding to that voxel, and the change is relatively small. (For example, using the values from Table 2.1, a drop in blood perfusion rate to zero at a given voxel changes the value of the diagonal element of A corresponding to that voxel by less than 4%, and leaves all other elements unchanged). This small difference allows $(A_0 + A_a)^{-1}$ to be approximated:

$$(A_0 + A_a)^{-1} \approx A_0^{-1} - A_0^{-1} A_a A_0^{-1} \quad (3.13)$$

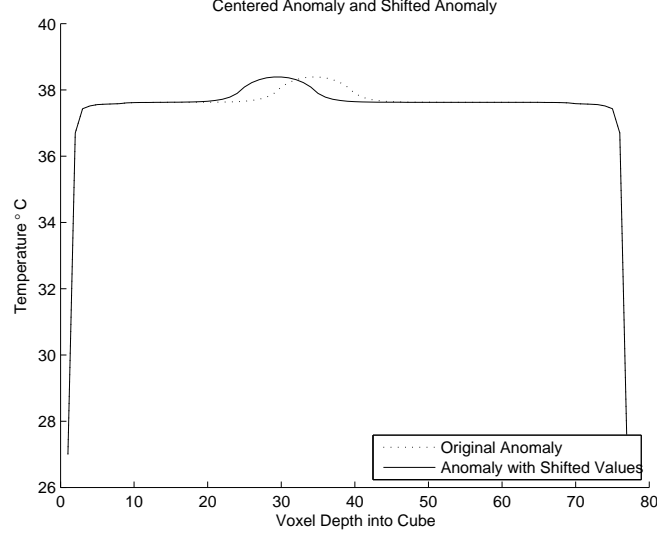


Figure 3.1. 1-D View of abnormal temperature profiles where the anomaly occurs at two different locations.

The term $(\underline{b}_a - A_a \underline{T}_0)$ in 3.12 can be expanded as $\sum_{\underline{v} \in V_a} \alpha(\underline{v}) \underline{\delta}_v$ where V_a is a set of anomalous voxels, $\underline{\delta}_v$ is the unit vector of the voxel \underline{v} and $\{\alpha(\underline{v})\}$ is some set of coefficients. (This follows from the fact that the A_a has non-zero columns of the form $\{C(\underline{v})\delta_{\underline{v}}, \underline{v} \in V_a\}$). The anomalous temperature field then satisfies:

$$\begin{aligned} \underline{T}_a &\approx (A_0^{-1} - A_0^{-1} A_a A_0^{-1}) \sum_{\underline{v} \in V_a} \alpha(\underline{v}) \underline{\delta}_v \\ &= \sum_{\underline{v} \in V_a} \alpha(\underline{v}) (\underline{h}_v - A_0^{-1} A_a \underline{h}_v) \end{aligned} \quad (3.14)$$

Where \underline{h}_v represents the bio-heat impulse response due to the unit vector δ_v , $\underline{h}_v = A_0^{-1} \underline{\delta}_v$. Note that $A_a \underline{h}_v = \sum_{\underline{u} \in V} C(\underline{v}) \underline{h}_v(\underline{u}) \underline{\delta}_u$ where $\underline{h}_v(\underline{u})$ is the \underline{u}^{th} component of \underline{h}_v . Then:

$$\begin{aligned} \sum_{\underline{v} \in V_a} \alpha(\underline{v}) A_0^{-1} A_a \underline{h}_v &= \sum_{\underline{v} \in V_a} \sum_{\underline{u} \in V_a} \alpha(\underline{v}) C(\underline{v}) \underline{h}_v(\underline{u}) \underline{h}_u \\ &= \sum_{\underline{v} \in V_a} \sum_{\underline{u} \in V_a} \alpha(\underline{u}) C(\underline{u}) \underline{h}_u(\underline{v}) \underline{h}_v \end{aligned} \quad (3.15)$$

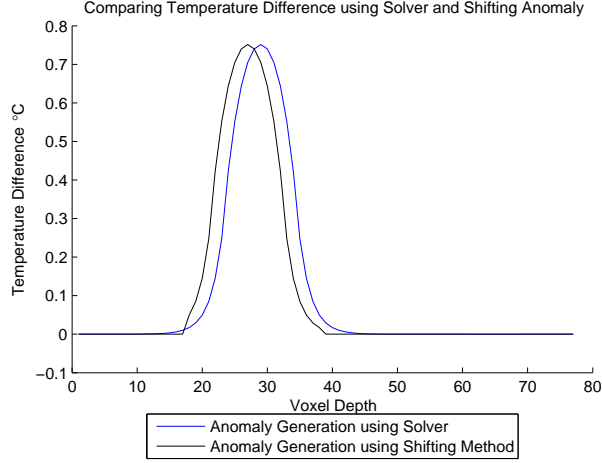


Figure 3.2. Comparison of temperature anomalies generated using the matrix solver and shifting the anomaly.

So that:

$$\underline{T}_a \approx \sum_{\underline{v} \in V_a} \left[\alpha(\underline{v}) - \sum_{\underline{u} \in V_a} \alpha(\underline{u}) C(\underline{u}) h_{\underline{v}}(\underline{u}) \right] \underline{h}_{\underline{u}} \quad (3.16)$$

From the equation above, anomalous temperature fields can be approximated as linear combinations of impulse responses to the nominal PBE with inputs in the anomalous region. Suppose that the entire volume V_a can be broken up into disjoint blocks such that $V_a = \sum_m V_{a,m}$. Then equation 3.16 becomes:

$$\underline{T}_a \approx \sum_m \left[\sum_{\underline{v} \in V_{a,m}} \left[\alpha(\underline{v}) - \sum_{\underline{u} \in V_a} \alpha(\underline{u}) C(\underline{u}) h_{\underline{v}}(\underline{u}) \right] \underline{h}_{\underline{v}} \right] \quad (3.17)$$

While the anomalous field due to an anomaly confined to $V_{a,m}$ is:

$$\underline{T}_{a,m} = \sum_{\underline{v} \in V_{a,m}} \left[\alpha(\underline{v}) - \sum_{\underline{u} \in V_{a,m}} \alpha(\underline{u}) C(\underline{u}) h_{\underline{v}}(\underline{u}) \right] \underline{h}_{\underline{v}} \quad (3.18)$$

Comparing to equation 3.35, we see that $\underline{T}_a \approx \sum_m \underline{T}_{a,m}$. If we include coefficients $\{\psi(m)\}$ to allow for a better match, then the anomalous temperature field can be

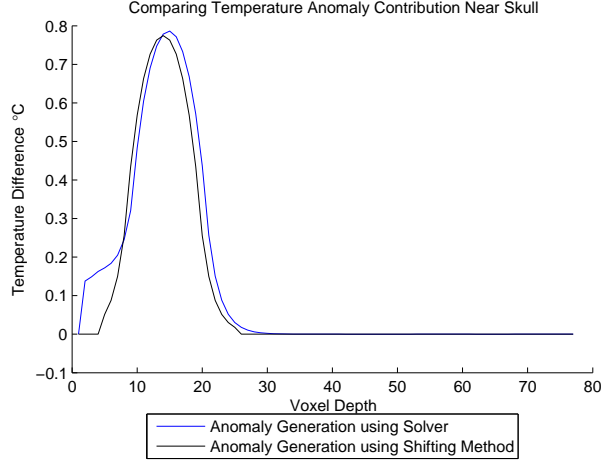


Figure 3.3. Comparison of temperature anomalies generated using the matrix solver and shifting the anomaly closer to the skull

approximated as:

$$\underline{T}_a \approx \sum_m \psi(m) \underline{T}_{a,m} \quad (3.19)$$

where $\psi(m)$ is a set of non-negative weights that optimize the approximation. The brightness temperature anomaly signature then satisfies:

$$\underline{s}_a \approx \sum_m \psi(m) W^* \underline{T}_{a,m} = \sum_m \psi(m) \underline{s}_{a,m} \quad (3.20)$$

where $\underline{s}_{a,m}$ are the generated brightness temperature anomaly signatures.

3.2.2 GLR Test Using Signatures

We now formulate an anomaly detector using the generated signature dictionary. Define the true anomaly brightness temperature signature to be $\underline{s}_a = W^* \underline{T}_a$:

$$\begin{aligned} H_0 : \underline{T}_B &= W^* \underline{T}_0 + \underline{T}_n \\ H_1 : \underline{T}_B &= W^* \underline{T}_0 + \underline{T}_n + \underline{s}_a \end{aligned} \quad (3.21)$$

As previously, the nominal brightness temperature W^*T_0 is subtracted from T_B to give the vector \underline{U} that satisfies hypothesis:

$$\begin{aligned} H_0 : \underline{U} &= \underline{T}_n \sim N(0, \sigma^2 I) \\ H_1 : \underline{U} &= \underline{T}_n \sim N(\underline{s}_a, \sigma^2 I) \end{aligned} \quad (3.22)$$

Applying the generalized likelihood approach, the test statistic of the log-likelihood ratio is:

$$\begin{aligned} t &= \langle \underline{U}, \hat{\underline{s}}_a \rangle - \frac{1}{2} \langle \hat{\underline{s}}_a, \hat{\underline{s}}_a \rangle \\ &= \langle \underline{U}, \hat{\underline{s}}_a \rangle - \frac{1}{2} \|\hat{\underline{s}}_a\|^2 \end{aligned} \quad (3.23)$$

where $\hat{\underline{s}}_a$ is the maximum likelihood estimate of \underline{s}_a . We have investigated two methods for determining $\hat{\underline{s}}_a$. First, a linear combination of signatures from the dictionary is used (following equation 3.20) and second the signature in the dictionary with the highest correlation to the observed values is selected as the anomaly signature estimate.

To estimate the anomalous signature using a linear combination, let S contain columns of signatures $\{\underline{s}_{a,m}\}$. The ML estimate of the coefficients in equation 3.20 is the solution to the problem:

$$\text{Find } \underline{\psi} \text{ that minimizes } \|\underline{U} - S\underline{\psi}\|^2 \text{ such that } \psi(m) \geq 0 \text{ for } m = 1, \dots, M \quad (3.24)$$

where $\underline{\psi}$ is a set of non-negative coefficients.

By using Kuhn Tucker conditions once again, the coefficient vector $\underline{\psi}$ must satisfy:

$$S^*S\underline{\hat{\psi}} = S^*\underline{U} + \underline{d}, \text{ where } d(m) \geq 0 \text{ for } m = 1, \dots, M \text{ and } d(m) = 0 \text{ when } \hat{\psi}(m) > 0 \quad (3.25)$$

The next step is to solve for $\underline{\hat{\psi}}$ by using the restricted inverse of S^*S .

$$\underline{\hat{\psi}} = (S^*S)_r^{-1}S^*\underline{U} + (S^*S)_r^{-1}\underline{d} \quad (3.26)$$

The right hand side of the equation can be broken into two terms, $(S^*S)_r^{-1}S^*\underline{U}$ and $(S^*S)_r^{-1}\underline{d}$. Then combined to solve for the coefficients. We will first solve for $(S^*S)_r^{-1}S^*\underline{U}$. Finding the restricted inverse may prove difficult so instead the term is rewritten in terms of eigenvalues $\{\lambda_j\}$ and eigenvectors $\{\underline{\phi}_j\}$ of the full-rank ($K \times K$) matrix SS^* :

$$(S^*S)S^*\underline{\phi}_j = \lambda_j S^*\underline{\phi}_j \quad (3.27)$$

(Note that $\lambda_j > 0$ for all $j = 1, \dots, K$). Equation 3.27 can be rewritten as:

$$(S^*S)\rho_j = \lambda_j \rho_j \quad (3.28)$$

where

$$\rho_j = \frac{1}{\sqrt{\lambda_j}} S^*\underline{\phi}_j \quad (3.29)$$

Then since $S^*\underline{U} = \sum_{j=1}^L \langle S^*\underline{U}, \rho_j \rangle \rho_j$ we have:

$$\begin{aligned} (S^*S)_r^{-1}S^*\underline{U} &= \sum_{j=1}^L \frac{1}{\sqrt{\lambda_j}} \langle S^*\underline{U}, \rho_j \rangle \rho_j \\ &= \sum_{j=1}^L \langle S^*\underline{U}, \frac{1}{\sqrt{\lambda_j}} S^*\underline{\phi}_j \rangle \frac{1}{\sqrt{\lambda_j}} S^*\underline{\phi}_j \\ &= \sum_{j=1}^L \frac{1}{\lambda_j} \langle S^*\underline{U}, S^*\underline{\phi}_j \rangle S^*\underline{\phi}_j \\ &= \sum_{j=1}^L \frac{1}{\lambda_j} \langle \underline{U}, SS^*\underline{\phi}_j \rangle S^*\underline{\phi}_j \end{aligned} \quad (3.30)$$

Define Φ as a $K \times K$ matrix whose columns are $\{\underline{\phi}_k\}$ and Λ the diagonal matrix of eigenvalues $\{\lambda_k\}$, then equation 3.30 above can be rewritten as:

$$(S^*S)_r^{-1}S^*\underline{U} = S^*\Phi\Lambda^{-1}\Phi^*\underline{U} \quad (3.31)$$

The term $(S^*S)_r^{-1}\underline{d}$ can then be found similarly:

$$\begin{aligned} (S^*S)_r^{-1}\underline{d} &= \sum_{j=1}^L \frac{1}{\lambda_j} \langle d, \rho_j \rangle \rho_j \\ &= P\Lambda^{-1}P^*\underline{d} \end{aligned} \quad (3.32)$$

where P is the $M \times K$ matrix whose columns are $\underline{\rho}_k$. Therefore:

$$\hat{\underline{\psi}} = S^*\Phi\Lambda^{-1}\Phi^*\underline{U} + P\Lambda^{-1}P^*\underline{d} \quad (3.33)$$

where $d_k \geq 0, k = 1, \dots, K$ and $d_k = 0$ if $\psi_k > 0$.

To find $\hat{\underline{\psi}}$ from equation 3.33 we let $M_0 = \{m : \{S^*\Phi\Lambda^{-1}\Phi^*\underline{U}\}_m < 0\}$ and let \underline{B}_m denote the m^{th} column of $P\Lambda^{-1}P^*$. Then we set:

$$\begin{aligned} (i) \quad & d(m) = 0 \text{ if } m \notin M_0 \\ (ii) \quad & \{S^*\Phi\Lambda^{-1}\Phi^*\underline{U}\}_m = \sum_{l \in M_0} B_l(m)d(l), m \in M_0 \end{aligned} \quad (3.34)$$

We solve the set of equations (3.34 (ii)) for $\{d(m), m \in M_0\}$ and set $\hat{\underline{\psi}} = S^*\Phi\Lambda^{-1}\Phi^*\underline{U} + P\Lambda^{-1}P^*\underline{d}$. Then $\hat{\underline{s}}_a = S\hat{\underline{\psi}}$ is used to form the GLR test statistic (3.23).

The approach outlined above estimates the anomaly signature under H_1 by a linear combination of all signatures in the dictionary. One potential problem with this approach is that since there are many more dictionary entries than observation components, there are too many degrees of freedom - we can find a linear combination of

signatures that matches almost any positive deviation from the nominal temperature, so the test statistic (3.34) is not much different from that of equation 3.12.

As an alternative, we can estimate \underline{s}_a by the one signature in the dictionary that best matches \underline{U} . That is, define:

$$\hat{\underline{s}}_a = \underset{m, \psi > 0}{\operatorname{argmin}} \|\underline{U} - \psi \underline{s}_{a,m}\|^2 \quad (3.35)$$

Since the $\underline{s}_{a,m}$ are normalized, this leads to:

$$\hat{\underline{s}}_a = \max\{\max_x \langle \underline{U}, \underline{s}_{a,m} \rangle, 0\} \quad (3.36)$$

We can then use this in equation (3.23) to generate one more detection test statistic.

3.2.3 Anomaly Location Estimation Using Signatures

The set of signatures can also be used to estimate the location of an anomaly. As stated previously, the number of radiometric measurements is significantly smaller than the number of unknowns and makes the reconstruction of a temperature profile impossible. Selecting the signature with the highest correlation is equivalent to selecting the anomalous temperature profile that produced the brightness temperature with the highest correlation. Instead of reconstructing the entire profile, the goal becomes the selection of a profile that mostly likely resembles the observation. The center of the most highly correlated signature entry then becomes an estimate of the true anomaly location. For cases where there is more than one anomaly present, the correlation from each observation point could be calculated separately.

3.3 Conclusion

This chapter described two detection algorithms that used anatomical information. The first method only used the nominal brightness temperature. The second and

method used sets of signatures to estimate the anomalous observation. The estimate of the signature can be found by finding the linear combination of signatures or choosing the signature with the largest correlation with the observation. An energy based detection algorithm is also derived when anatomical information is not available in order to compare the derived detection methods introduced. The simulation results for each of the detection methods and estimation results are presented in Chapter 4.

CHAPTER 4

DETECTION AND ESTIMATION RESULTS

4.1 Cube Model Simulation Results

In simulations, the detection algorithms derived in Chapter 3 were executed to compare their performance rates. We expected that algorithms that include anatomical knowledge will produce better detection results than the energy-based algorithm. Simulations were run on the same cubic tissue model used to construct the temperature profiles and weighting functions in Chapter 2. To represent an anomaly, an ischemic condition was represented by setting the blood perfusion rate to zero in a 1000 voxel region. Temperature brightness measurements were calculated by taking the inner product of the weighting functions and the temperature profiles.

To generate Receiver Operative Characteristics (ROCs), noise and variation needed to be introduced into simulations. To achieve this, 500 nominal and abnormal brightness temperatures were generated by adding varying Gaussian noise to the normal and abnormal brightness temperatures. The same noise generator was used for each detection method to ensure fair comparison across the detection methods. Test statistics were calculated using the generated brightness temperatures for all hypothesis frameworks/detection algorithms. ROCs were generated by varying the threshold under each detection method, γ , and counting the test statistic values under the null hypothesis, H_0 , that fell above the threshold (giving the false alarm rate). The test statistic values under the abnormal hypothesis, H_1 , that fell above the threshold were also counted (giving the detection rate).

A set of 125 signatures were pre-calculated for use in the detection algorithms and location estimation. A 10x10x10 anomaly was observed in the center of the cube and although the anomaly occurs in an 1000 voxel region, the neighboring voxels also show an increase in temperature. The anomalous contribution was isolated to a 16x16x16 voxel region. Each signature was generated by shifting the 16x16x16 voxel region throughout the 3D temperature profile. The anomaly contribution was only allowed to occur within brain matter. The brightness temperature for each profile was calculated and the difference from the nominal brightness temperature was found. Each set of differences was then normalized.

While generating signatures, the location of each anomaly is recorded. The signature with the highest correlation is selected as the estimated anomaly location. The euclidean error is calculated between the actual and the estimated locations. We also estimated the anomalous location with no radiometric noise. The estimated location with no radiometric noise provides the best possible estimation and helped to determine if estimation results with noise were acceptable.

Four radiometric views were chosen with three frequencies (2.45 GHz, 3.5 GHz, and 4.5 GHz) observed at each position, resulting in 12 radiometric measurements. Each radiometric view was centered in the face plane of the cube. Assuming that the anomaly can occur anywhere in the model lowers detection rates. However, this assumption is feasible if the location of an anomaly is unknown [23]. ROC results for a 10x10x10 anomaly placed 16mm from the skin's surface under .05°C noise variation (Figure 4.1). The location was slightly off center by 6 voxels (12 mm). Estimating the signature using the highest correlated signature produces detection rates of 85 percent for 10 percent false alarm. Using correlation outperforms the energy based method by 45 percent. All detection methods that incorporate anatomical information produce better results than the energy based method.

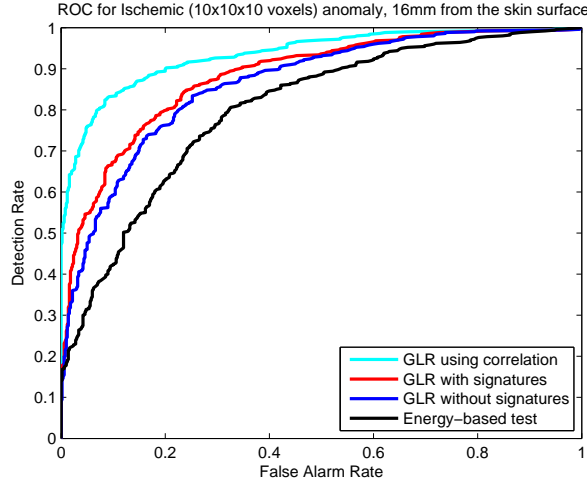


Figure 4.1. ROC of 16mm deep 10x10x10 anomaly in Cube model with $.05^{\circ}\text{C}$ standard deviation.

For over 90 percent of simulations, the location distance error was 4 voxels (Figure 4.2). The closest location in the signature set is 4 voxels which proves that our method to estimate an anomaly location produces decent results. The detection rates and estimation results were also found for $.1^{\circ}\text{C}$ noise error (Figures 4.3 and 4.4).

4.2 Zubal Model Simulation Results

The cube model's dimensions are comparable to an infant child and were originally used to determine the detection on a small model. The detection algorithms were also performed on an adult head; the Zubal head model. A set of 1335 signatures were created by shifting a 10x10x10 anomaly throughout the brain matter in the Zubal model. In the cube model, the anomalous temperature was shifted strictly within the brain matter. In the Zubal model, however, there are pockets of CSF throughout the brain matter so the anomaly needs to be shifted throughout the brain and csf tissue types. For each anomalous case, the location was estimated and the euclidean distance error was calculated. The best estimate was also found by not adding noise to

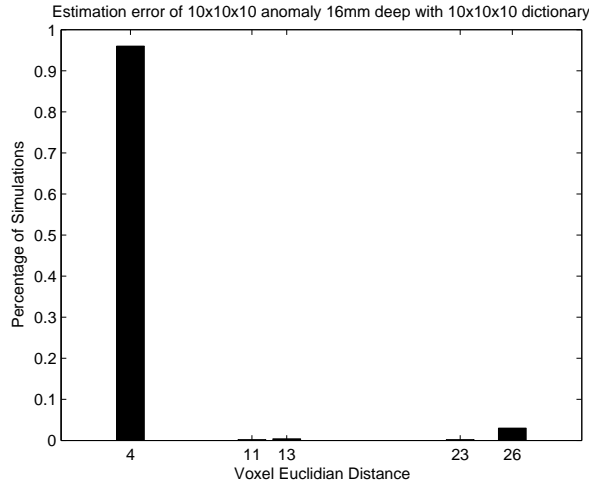


Figure 4.2. Euclidean error estimation results of 16mm deep 10x10x10 anomaly in Cube model with .05°C standard deviation.

the observed brightness temperatures. This helped to determine the best achievable estimate based on the set of signatures.

ROCs were generated for all proposed detection methods assuming varying degrees of noise error. Anomalies were placed at various depths to determine the limits of detection based on anomaly depth. Once again, the detection algorithms that include signatures in the detection process produce the best detection results. Using anatomical information in both detection algorithms produces better results than the energy based method.

The estimation location results appear to follow a pattern in terms of the euclidean distance error. This was also true in the Cube estimation results. This is because a noise seed generator is being used in Matlab. As a result, the noise results for 500 scenarios are all the same. This was done to guarantee that the detection algorithms were being compared under the same conditions. The seed can be removed or adjusted to observe other random noise scenarios.

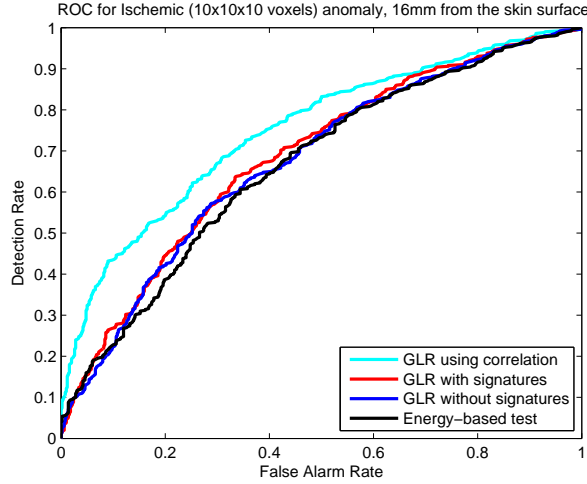


Figure 4.3. ROC of 16 mm deep 10x10x10 anomaly in Cube model with $.1^{\circ}\text{C}$ standard deviation.

4.3 Discussion of Results

4.3.1 Effects of Radiometric Noise

The radiometric noise has a significant impact in the detection algorithms and the ability to detect anomalies with a low false alarm rate. Detection results are promising when the standard deviation is $.05^{\circ}\text{C}$ in the Cube model which has a detection rate of 80 percent for a false alarm rate of 10 percent (Figure 4.5). Increasing the standard deviation to $.1^{\circ}\text{C}$ reduces detection rates to 40 percent for a false alarm rate of 10 percent (Figure 4.7). Based on these results, minimizing the radiometric noise will be an important design requirement in order to use radiometry in medical applications.

The radiometric noise also impacts the location estimation results in a similar manner. When the standard deviation is $.1^{\circ}\text{C}$ the percentage of results with the minimal euclidean distance error is about 74 percent (Figure 4.8). However, when the standard deviation is $.05^{\circ}\text{C}$, the minimal euclidean distance is found for 96 percent of the cases (Figure 4.6). The minimal euclidean error is 4 voxels in both scenarios. Based on the signature dictionary, there were no other entries in the dictionary that were closer to the actual location of the anomaly than the estimated location.

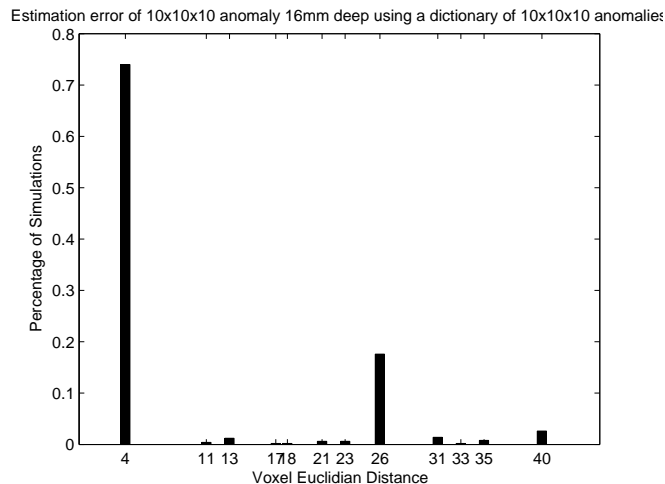


Figure 4.4. Euclidean error estimation results of 16mm deep 10x10x10 anomaly in Cube model with $.1^{\circ}\text{C}$ standard deviation.

Detection results for the cube model are better than those for the Zubal model. This is most likely due to the method in which weighting functions were acquired. In the cube model, the waveguide was flush against the side of the cube and therefore power was deposited in a focused region. For the Zubal model, the waveguide was against the back of the head model which curved and there were open areas due to the waveguide dimensions that allowed power to escape. For future work, the waveguide needs to be made smaller to focus the power reception and also improve feasibility in the medical environment. This can be done by inserting a ceramic into the waveguide. For example, the S-band waveguide would reduce in size from 7.620 by 3.819 cm to 1.14 by .212 cm [24].

4.3.2 The Impact of the Radiometer Location

In the cube results above, the anomaly was shifted slightly off center (12 mm) from the radiometer view. If the anomaly occurs in direct view of the radiometer the detection results improve by 15 percent to 95 percent detection rate for 10 percent

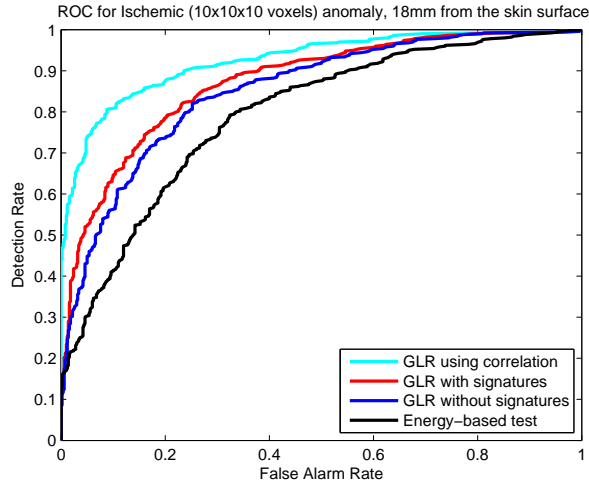


Figure 4.5. ROC of 18mm deep 10x10x10 anomaly in Cube model with $.05^{\circ}\text{C}$ standard deviation.

false alarm rate (Figure 4.15). Based on these results, some type of radiometer array can be used to increase detection of anomalies.

4.3.3 Effects of Anomaly Depth

The depth of the anomaly will also impact detection and estimation results. Anomalies that occur at a higher depth have less weight in the weighting function and have less impact on the radiometric readings. For this analysis, all anomalies were centered in radiometer’s viewing position. At 20mm deep, the detection rate is 77 percent for 10 percent false alarm rate (Figure 4.16). At 22mm deep, the detection rate reduces by 22 percent to 55 percent for a 10 percent false alarm rate (Figure 4.17).

4.3.4 Effects of Anomaly Size

Larger sized anomalies cause larger increases in temperature. Detection of larger anomalies is easier compared to smaller sized anomalies. Figure 4.18 shows the ROC for an anomaly that is 6x6x6 voxels. Figure 4.19 shows the ROC for an anomaly that

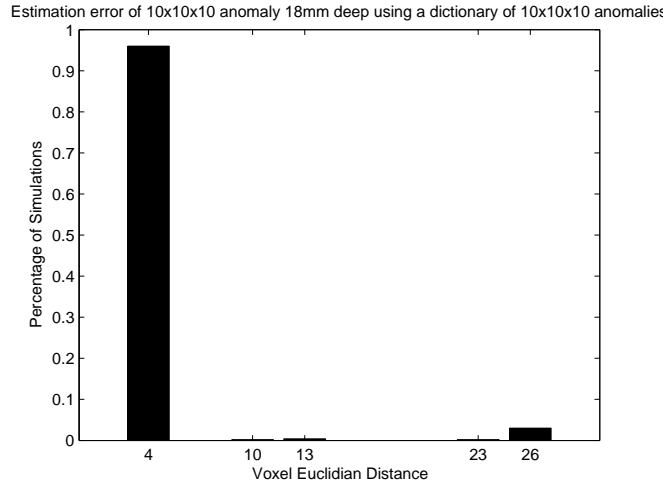


Figure 4.6. Euclidean error estimation results of 18mm deep 10x10x10 anomaly in Cube model with .05°C standard deviation.

is 8x8x8 voxels. Figure 4.20 shows the ROC for an anomaly that is 10x10x10 voxels. In all cases, the edge of the anomaly occurs at the same depth (16mm from the skin’s surface). However, the 10x10x10 anomaly has better detection results compared to the 8x8x8 anomaly for a 10 percent false alarm rate.

4.3.5 Effects of Signature Size

The size of the dictionary also impacts the detection rates for the correlation method. Generating signatures with smaller sized anomalies will not be helpful because smaller anomalies are harder to detect as shown in Figures 4.18 to 4.20. Larger sized dictionaries can be created by shifting the anomaly in the 3D model by different increments. Two additional sets of signatures were produced by shifting the anomaly every 5 and 8 voxels. Shifting by 5 voxels produces 1331 signatures and shifting by 8 voxels produces 343 signatures. For analysis, an 8x8x8 anomaly was placed 16mm deep in the cube model. By using a larger set of signatures the detection rate improves by 6 percent (Figure 4.21). The set of 343 signatures slightly out performs the set with 1331 signatures, however, there is little difference between them. This

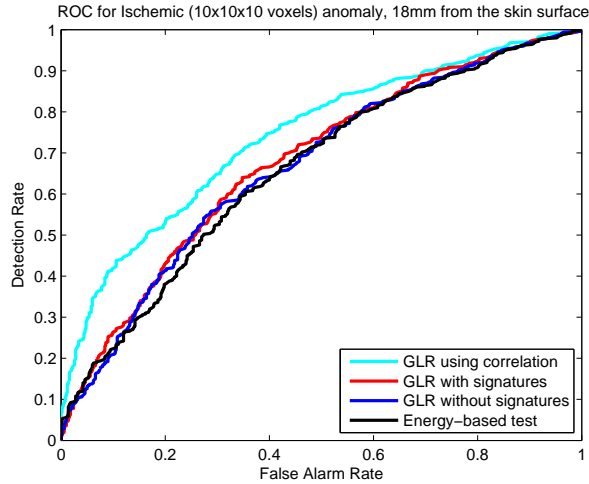


Figure 4.7. ROC of 18mm deep 10x10x10 anomaly in Cube model with $.1^{\circ}\text{C}$ standard deviation.

proves that increasing the signature size can be helpful but if the set is much larger, it does little to improve detection results.

4.4 Conclusion

This chapter presented the detection and estimation results based on the algorithms described in chapter 3. In each scenario, incorporating the anatomical information in the detection process produces better detection results. We also demonstrated how a set of signatures can be used to improve detection performance and estimate the location of an anomaly. Radiometric noise was found to play a significant part in detection rates and reducing noise will be a key design feature. The size of the anomaly, anomaly location, and signature sizes were varied to determine how detection rates are impacted.

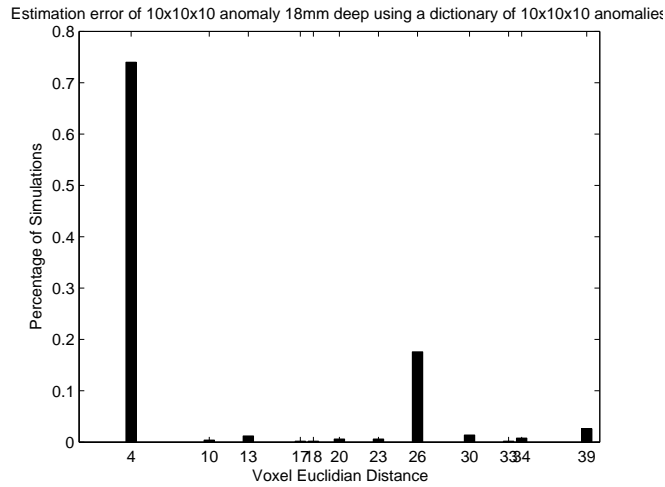


Figure 4.8. Euclidean error estimation results of 18mm deep 10x10x10 anomaly in Cube model with $.1^{\circ}\text{C}$ standard deviation.

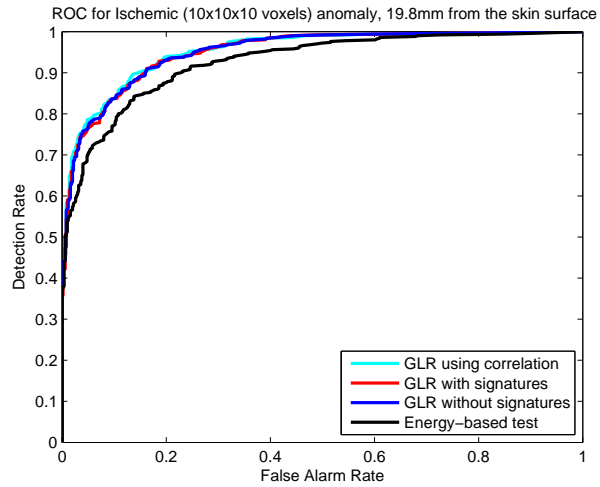


Figure 4.9. ROC of 19.8mm deep 10x10x10 anomaly in Zubal model with $.03^{\circ}\text{C}$ standard deviation.

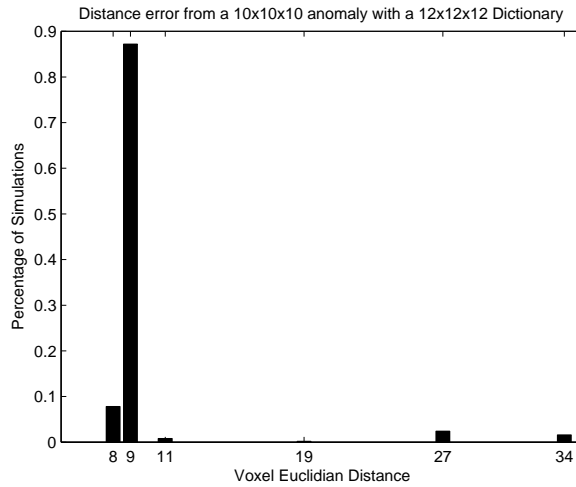


Figure 4.10. Euclidean error estimation results of 19.8mm deep 10x10x10 anomaly in Zubal model with $.03^{\circ}\text{C}$ standard deviation.

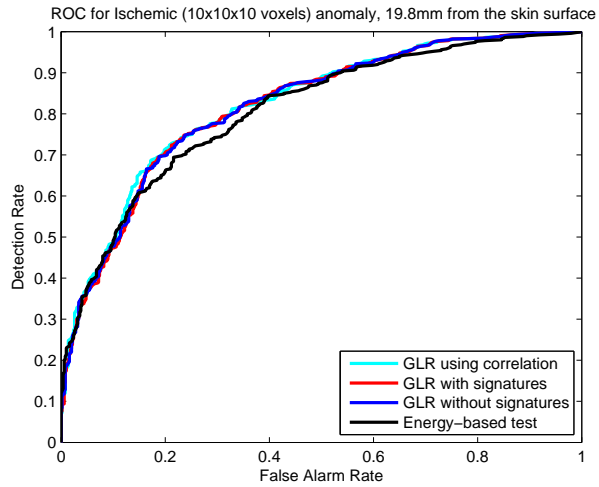


Figure 4.11. ROC of 19.8mm deep 10x10x10 anomaly in Zubal model with $.05^{\circ}\text{C}$ standard deviation.

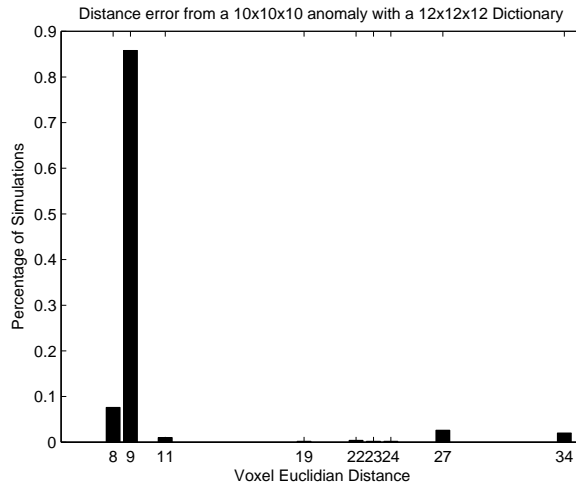


Figure 4.12. Euclidean error estimation results of 19.8mm deep 10x10x10 anomaly in Zubal model with $.05^{\circ}\text{C}$ standard deviation.

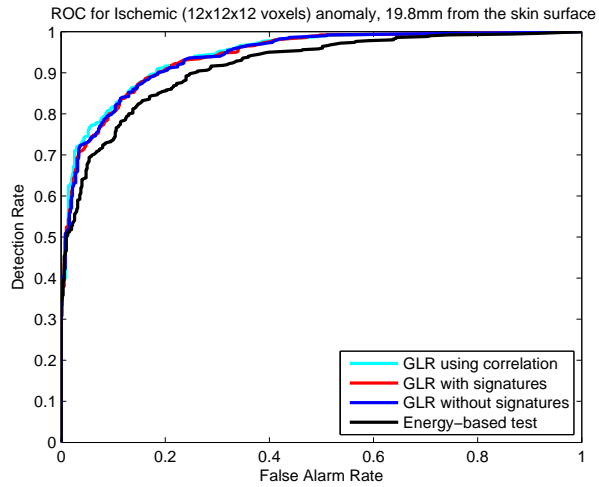


Figure 4.13. ROC of 19.8mm deep 12x12x12 anomaly in Zubal model with $.05^{\circ}\text{C}$ standard deviation.

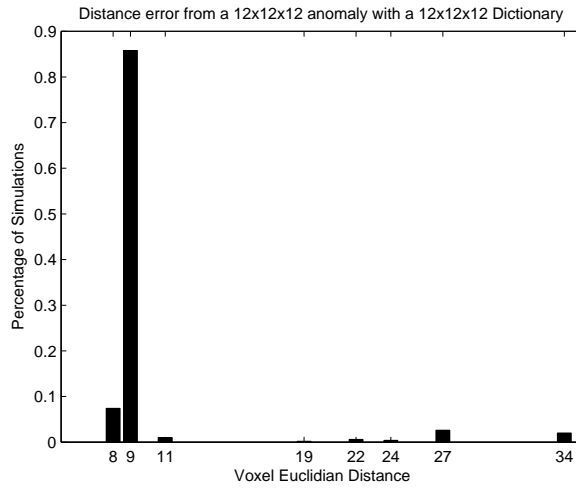


Figure 4.14. Euclidean error estimation results of 19.8mm deep 12x12x12 anomaly in Zubal model with $.05^{\circ}\text{C}$ standard deviation.

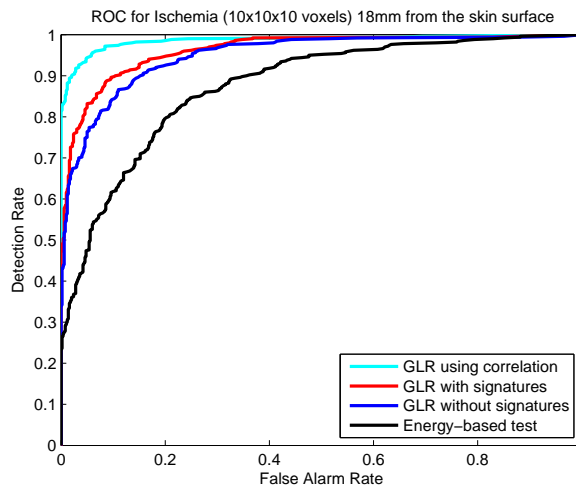


Figure 4.15. ROC of a *centered* 18mm deep 10x10x10 anomaly in Cube model with $.05^{\circ}\text{C}$ standard deviation.

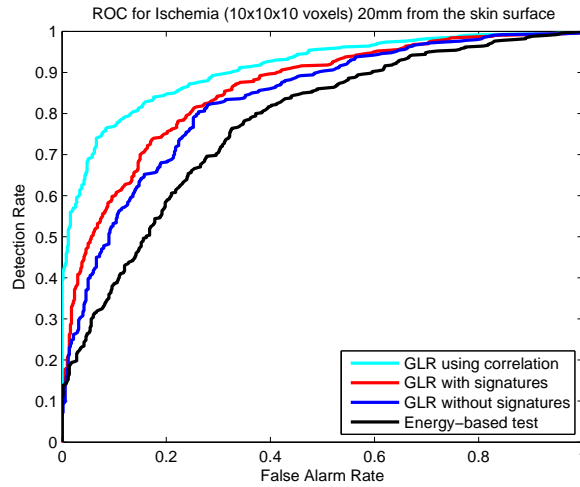


Figure 4.16. ROC of a *centered* 20mm deep 10x10x10 anomaly in Cube model with .05°C standard deviation.

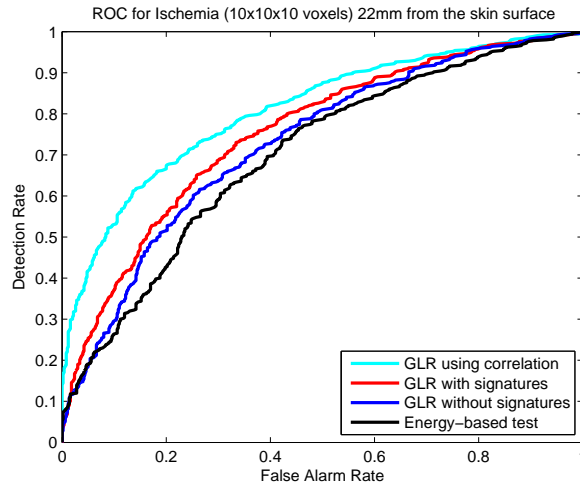


Figure 4.17. ROC of a *centered* 22mm deep 10x10x10 anomaly in Cube model with .05°C standard deviation.

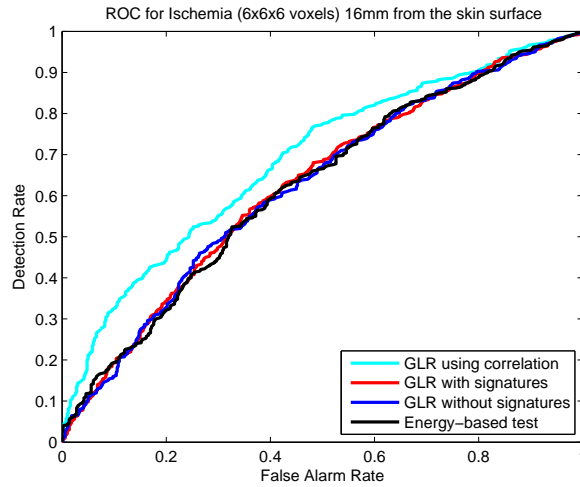


Figure 4.18. ROC of a *centered* 16mm deep 6x6x6 anomaly in Cube model with .05°C standard deviation.

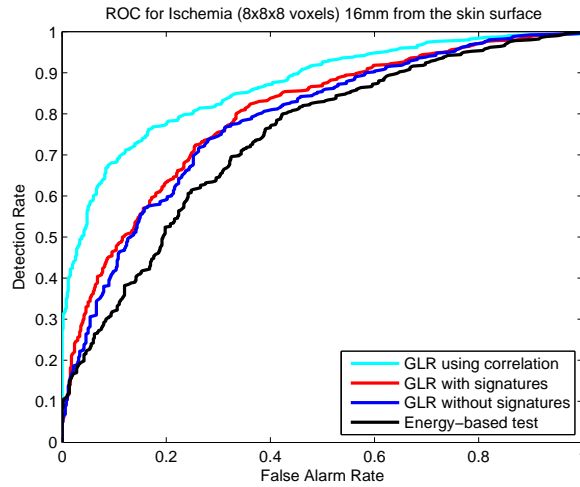


Figure 4.19. ROC of a *centered* 16mm deep 8x8x8 anomaly in Cube model with .05°C standard deviation.

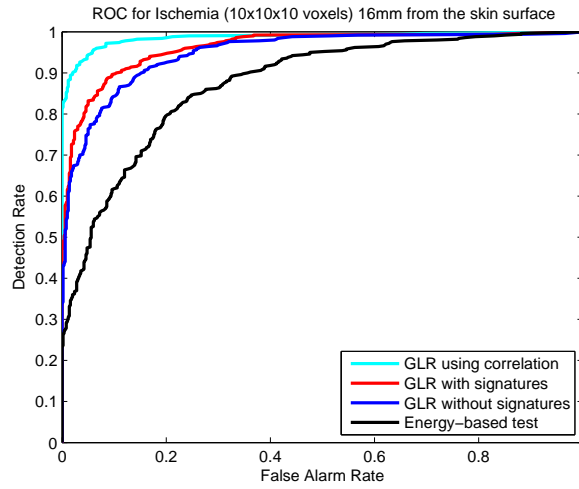


Figure 4.20. ROC of a *centered* 16mm deep 10x10x10 anomaly in Cube model with .05°C standard deviation.

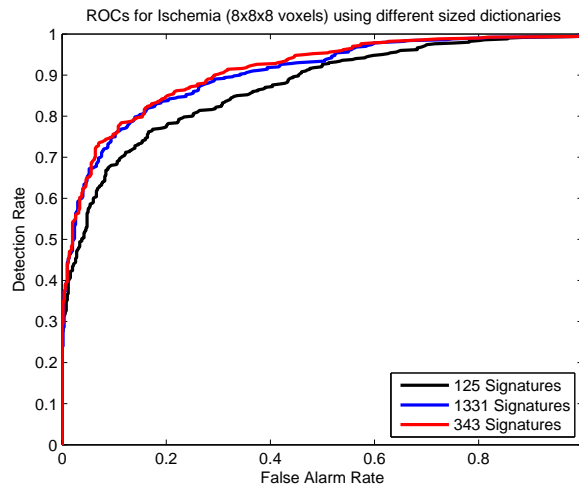


Figure 4.21. ROCs of a *centered* 16mm deep 8x8x8 anomaly in Cube model with .05°C standard deviation using different sized signature sets.

CHAPTER 5

EFFECTS OF PARAMETER VARIATIONS

The nominal brightness temperature is calculated by using the set of physiological parameters in Table 2.2. However, different papers have different parameter values and variation is expected among the general population. Parameters may also vary within a person depending on the time of day, whether a person recently ate, stress, and other factors that cannot be precisely accounted for. The anomaly detection algorithms described in Chapter 3 rely on the fact that nominal variations in physiological properties cause temperature variations smaller than actual anomalies. If these variations are large, then the constructed detection algorithm would not work because it would not detect the difference between an anomaly and nominal temperature readings.

Parameter variation can be categorized into two categories, systematic and noise errors. Systematic errors are viewed as a consistent variation that takes place in individuals that are different from the nominal values. Noise variations are interpreted as random parameter variations across the observed region. This chapter covers the impact of variations on the different physiological parameters and presents possible methods of reducing uncertainty.

5.1 Systematic Error Analysis

Using the cube model, parameters were given a constant variation of error and the resulting brightness temperatures were calculated. Results show that the difference between the original brightness temperature and the temperature under systematic

Table 5.1. Variation caused by systematic parameters on the nominal brightness temperature measurements at different frequencies.

Systematic Error	2.45 GHz	3.5 GHz	4.5 GHz
-20%	0.0280	0.0083	0.0228
-10%	-.0106	.0022	-.0087
+10%	.0065	.0001	.0054
+20%	-0.0106	0.0012	-0.0088

variations are small (Table 5.1). Literature has also found that although variation is expected, the PBE still provides a good model that can match expectations [9].

5.1.1 Dielectric Properties

The average dielectric systematic variation that is expected to occur does not have a significant impact on the weighting function measurements. This was shown in [18], [1], and [17].

5.1.2 Thermal Conductivities

Thermal conductivity does vary among the different tissue types, however, within the same tissue, thermal conductivity does not change by a significant amount. This also applies to the thermal conductivity values in the brain. Although there are different tissues types in the brain (such as grey and white matter), the thermal properties of the brain are consistent [21]. The difference between an abnormal brightness temperature and measurements with errors in thermal conductivity were also calculated (Table 5.2). Anomalous regions may have other physiological deviations than just the blood perfusion rate.

5.1.3 Tissue Layer Thicknesses

Accurate tissue layer thickness information is important for calculating correct weighting functions [18]. If tissue layer thicknesses are unknown, Ultrasound measurements can be used to make measurements and reduce errors[4], [22]. Tissue

Table 5.2. Variation between the abnormal brightness temperature measurements and brightness temperatures with systematic errors in thermal conductivity within the anomalous region.

Error	2.45 GHz	3.5 GHz	4.5 GHz
-20%	0.0096	-0.0151	-0.02
-10%	-0.0046	-0.0074	-0.0097
+10%	0.0047	0.0074	0.0095
+20%	0.0093	0.0149	0.0187

accuracy is important because errors will impact the weighting functions and radiometric measurements. If tissue thickness is incorrect, it is possible to give more weight to areas in the model that do not actually contribute a significant amount to the weighting function.

5.1.4 Metabolic Rate

The metabolic rate throughout the body is known to vary. Even the metabolic rate in the brain can change based on the activity in the brain. However, Collins showed the greatest cause to temperature deviation occurs when the blood perfusion rate varies from the norm [3]. This is also observed by calculating the difference in brightness temperatures when metabolic rates deviate from the norm within the anomalous region (Table 5.3). These deviations show that the greatest effect on the temperature are variations in the blood perfusion rate. However, since the best detection rates are seen when the radiometric noise is $.05^{\circ}\text{C}$ (for the cube model), metabolic variation may impact the detection rate if the noise cannot be reduced.

5.1.5 Blood Perfusion Rate

Previous studies have also shown that changes in the blood perfusion rate cause significant temperature profile errors [32]. For this reason, changes in the nominal values were used to represent anomalies. The effects of these changes can be seen in the detection algorithms and location estimation [23], [24]. Also, the uncertainty of the blood perfusion rate can be reduced by using doppler ultrasound [30].

Table 5.3. Variation between the abnormal brightness temperature measurements and brightness temperatures with systematic errors in metabolic rate within the anomalous region.

Error	2.45 GHz	3.5 GHz	4.5 GHz
-30%	-0.0187	-0.0353	-0.0345
-20%	-0.0124	-0.0235	-0.023
-10%	-0.0062	-0.0118	-0.0115
+10%	0.0063	0.0017	0.0115
+20%	0.0125	0.0235	0.023
+30%	0.0186	0.0352	0.0345

5.2 Noise Error Analysis

To observe nominal variations, temperature profiles of the cube were generated by varying the parameter values used to solve the PBE (i.e. thermal conductivity, blood perfusion rate, etc.) at each voxel. The only parameter that varied consistently was the metabolic rate which was uniformly distributed from 9000 to 11000 W/m^3 in the brain tissue. Other parameters were selected to vary from 10% to 50% error and tissues that had parameter values set to zero did not change. The parameters were not smoothed between voxels but selected randomly on a uniform distribution range based on the error percentage selected. The nominal temperature profile was then subtracted from the generated temperature profiles containing variations in the parameters.

The ischemic temperature profile difference was calculated (Figure 3.2) and showed a maximum temperature difference up to $.7^{\circ}C$ whereas the difference with 10% variation in parameters is less than $0.1^{\circ}C$ (Figure 5.1). Therefore, random variations in the nominal parameters are not expected to produce deviations from the nominal temperature that resemble anomalous temperature readings in the detection algorithm. The difference between the nominal brightness temperature and the brightness temperature as a result of 10% variation vary from $.0002$ to $.0012^{\circ}C$. With 20% variation, the changes increase to $.0047^{\circ}C$.

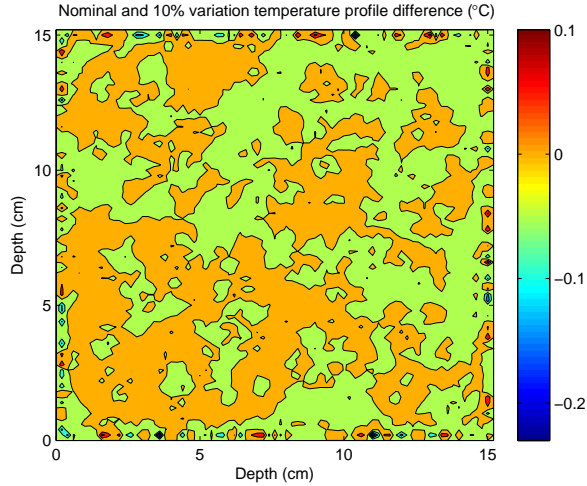


Figure 5.1. The temperature difference between profile with nominal parameters and profile with 10% random variations in nominal parameters.

5.3 Conclusion

This chapter analyzed the effects of systematic and random errors on the calculation of temperature profiles and the brightness temperature measurements. It may be possible to reduce error in model parameters such as tissue layer thicknesses and blood perfusion rates through the use of additional measurements such as pulse and doppler ultrasound [6]. Random errors produce minimal changes from the nominal results. Even errors in the anomalous region tend not to have a major impact on deviations from the nominal brightness temperature. The parameter with the greatest impact on the anomalous brightness temperature is the blood perfusion rate.

CHAPTER 6

CONCLUSION AND FUTURE WORK

The use of radiometry to detect anomalies in the human head have been investigated using simulations. Detection models were created using a hypothesis testing framework given that different amounts of a priori information is available. Detection rates improve when incorporating knowledge of the anatomical structure instead of using an energy-based approach. Using the anatomical model to pre-calculate signatures can further improve detection. Pre-calculated signatures can also be used to locate the anomalous region in the model. By locating the anomaly, there is no longer a need to estimate the entire temperature profile of the model.

We have shown that the detection rate of the radiometer is limited by the location of the anomaly and the noise variation of the radiometer will play a significant role in limiting detection results. Radiometry was previously investigated in medical applications for observing temperature deviations over time. By utilizing anatomical information, changes in temperature results can be detected in an instance. There is limited literature about the limitations of radiometry and this thesis detailed those results. The ability to reduce radiometric noise is a known goal in the microwave area. But the affect of the radiometric noise is presented in detail to provide a standard for allowable deviations that still allow for detection.

The ability to detect anomalies based on parameter variation was also investigated. Physiological parameters were varied by various percentages of error across the model and showed minimal changes in temperature that would affect the nominal brightness temperature. Systematic errors were observed to evaluate the effects of a consistent

variation which is expected among the general population. Again, the results showed that there were minimal affects to the brightness temperature.

We have studied using radiometry on head models, but expect that radiometry should perform equivalently or perhaps even better when observing other regions of the body. One application that should be investigated is breast cancer. Cancerous legions are known to have a higher temperature than normal tissue and this increase in temperature should be easier to capture using radiometry due to the tissue properties that allow for easier propagation.

BIBLIOGRAPHY

- [1] A. Levick and D. Land and J. Hand. Validation of microwave radiometry for measuring the internal temperature profile of human tissue. *Measurement Science and Technology* 22, 6 (June 2011).
- [2] B. Karaszewski and J.M. Wardlaw and I. Marshall and V. Cvorovic and K. Wartolowska and K. Haga and P. Armitage and M.E. Bastin and M.S. Dennis. Early brain temperature elevation and anaerobic metabolism in human acute ischaemic stroke. *Brain* 2009 132 (2009), 955–964.
- [3] C. M. Collins and M. B. Smith and Robert Turner. Model of local temperature changes in brain upon functional activation. *Journal of Applied Physics* 97 (2004), 2051 – 2055.
- [4] C. Y. Tan and B. Statham and R. Marks and P. Payne. Skin thickness measurement by pulsed ultrasound: its reproducibility, validation and variability. *British Journal of Dermatology* 106 (1982), 657–67.
- [5] D. A. Nelson. Invited Editorial on "Pennes' 1948 paper revisited". *Journal of Applied Physiology* 85 (1998), 2–3.
- [6] D. Ishigaki and K. Ogasawara and Y. Yoshioka and K. Chida and M. Sasaki and S. Fujiwara and K. Aso and M. Kobayashi and K. Yoshida and K. Terasaki and T. Inoue and A. Ogawa. Brain temperature measured using proton mr spectroscopy detects cerebral hemodynamic impairment in patients with unilateral chronic major cerebral artery steno-occlusive disease. *Stroke* 40 (2009), 3012–3016.

- [7] D. J. Brenner and E. J. Hall. Computed tomography - an increasing source of radiation exposure. *The New England Journal of Medicine* 357 (2007), 2277–2284.
- [8] D. Pozar. *Microwave Engineering*, vol. 3. Wiley, 2004.
- [9] E.H. Wissler. Pennes' 1948 paper revisited. *Journal of Applied Physiology* 85 (1988), 35 – 41.
- [10] F. Bardati and G. Marrocco. Time-dependent microwave radiometry for the measurement of temperature in medical applications. *IEEE* 52, 8 (Aug 2004), 1917–1924.
- [11] F. Bardati and S.Iudicello. Modeling the visibility of breast malignancy by a microwave radiometer. *IEEE Transactions on Biomedical Engineering* 55, 1 (Jan 2008), 214–221.
- [12] F. Rupich and I. Kyprianou and A. Badal and T. G. Schmidt. Energy deposition in the breast during ct scanning: quantification and implications for dose reduction. In *Proc SPIE Medical Imaging 2011* (2011), N. J. Pelc, E. Samei, and R. M. Nishikawa, Eds.
- [13] F.J. Gonzalez. Infrared imager requirements for breast cancer detection. In *Engineering in Medicine and Biology Society, 2007. EMBS 2007. 29th Annual International Conference of the IEEE* (Aug 2007), pp. 3312–3314.
- [14] G. Wezel-Meijler. *Neonatal Cranial Ultrasonography*. Prentice Hall, 2000.
- [15] G.A. Capraro, B.H. Nathanson, S. Jasienowski, M. Reiser, and F.S. Blank. Can the heat of localized soft tissue infections be quantified non-invasively using an infrared thermography camera? *Annals of Emergency Medicine* 52, 4 (2008). Supplement S157.

- [16] H.H. Pennes. Analysis of tissue and arterial blood temperatures in the resting human forearm. *J. Appl. Physiol* 1 (1948), 93–122.
- [17] J.B. Van de Kamer and N. Van Wieringen and A.A. De Leeuw and J.J. Lagendijk. The significance of accurate dielectric tissue data for hyperthermia treatment planning. *International Journal of Hypothermia* 17, 2 (2001), 123 – 142.
- [18] J.W. Hand and S. Van Leeuwen and G.M.J. Mizushina and J.B. Van de Kamer. Monitoring of deep brain temperature in infants using multi-frequency radiometry and thermal modeling. *Phys Med Biol* 46 (2001), 1885–1903.
- [19] K. Maruyama, S. Mizushina, and T. Sugiura. Feasibility of noninvasive measurement of deep brain temperature in newborn infants by multiple frequency microwave radiometry. *IEEE Trans Microw Theory Tech* 48, 11 (2000), 2141–2147.
- [20] K.L. Carr. Microwave radiometry: It’s importance to the detection of cancer. *IEEE Transactions on Microwave Theory and Techniques* 17, 12 (1989), 1862–1869.
- [21] L. Zhu and C. Diao. Theoretical simulation of temperature distribution in the brain during mild hypothermia treatment for brain injury. *Medical and Biological Engineering and Computing* 39, 6 (2001), 681–687.
- [22] M. M. Elahi and M. L. Lessard and S. Hakim and K. Watkin, J. Sampalis. Ultrasound in the assessment of cranial bone thickness. *The Journal of craniofacial surgery* 8, 3 (1997), 213–221.
- [23] P. Kelly and T. Sobers and B. St. Peter and P. Sequeira and G. Capraro. Temperature anomaly detection and estimation using microwave radiometry and anatomical information. In *Proc SPIE Medical Imaging 2011* (2011), Norbert J. Pelic, Ehsan Samei, and Robert M. Nishikawa, Eds., vol. 7961, SPIE.

- [24] P. Kelly and T. Sobers and B. St. Peter and P. Sequeira and G. Capraro. Microwave radiometric signatures of temperature anomalies in tissue. In *Proc SPIE Medical Imaging 2012* (2012), SPIE.
- [25] R.F. Harrington. *Time-Harmonic Electromagnetic Fields*. Wiley, 2001.
- [26] R.P. Clark and M.R. Goff. Medical thermography: Current status. In *Proc. SPIE 1320* (London, United Kingdom, 1990), Alan H. Lettington, Ed., vol. 1320, SPIE, pp. 242–250.
- [27] S. Gabriel and R.W. Lau and C. Gabriel. The dielectric properties of biological tissues: II measurements in the frequency range 10 hz to 20 ghz. *Physics of Medicine and Biology* 41, 11 (1996), 2251 – 2269.
- [28] S. Jacobsen and P.R. Stauffer. Nonparametric 1-d temperature restoration in lossy media using tikhunov regularization on sparse radiometry data. *IEEE Transactions on Biomedical Engineering* 50, 2 (2003), 178–188.
- [29] T. Butz, E. Dati, O. Divorra Escoda, M. Kunt, and P. Vandergheynst. Microwave temperature image reconstruction. *International Patent Application No. PCT/IB2006/052129* (Nov 1, 2007).
- [30] T. Jansson and H. W. Persson and K. Lindstrom. Estimation of blood perfusion using ultrasound. In *Proceedings of the Institution of Mechanical Engineers Journal of Engineering and Medicine* (1999), pp. 91 – 106.
- [31] T. Kubo and P. P. Lin and W. Stiller and M. Takahashi and H. Kauczor and Y. Ohno and H. Hatabu. Radiation dose reduction in chest ct: A review. *American Journal of Roentgenology* 190, 2 (2008), 335–343.
- [32] T. Sugiura and Y. Kouno and A. Hashizume and H. Hirata and J. W. Hand and Y. Okita and S. Mizushina. Five-band microwave radiometer system for non-

invasive measurement of brain temperature in new-born infants: system calibration and its feasibility. In *Proceedings of 26th IEEE International Conference of Engineering in Medicine and Biology* (2004), IEEE, pp. 2292 – 2295.

[33] T.K. Moon and W.C. Stirling. *Mathematical Methods and Algorithms*. Springer, 2007.

[34] www.remcom.com/x7.

[35] Y. Leroy and B. Bocquet and A. Mamouni. Non-invasive microwave radiometry thermometry. *Physiol Meas* 19, 2 (1998), 127–148.